SLAC-R-95-460
TOHOKU-HEP-95-01
TOHOKU-HEP-NOTE-95-06
UC-414

A MEASUREMENT OF QUARK AND GLUON JET DIFFERENCES AT THE Z^0 RESONANCE

Yoshihito Iwasaki

Stanford Linear Accelerator Center
Stanford University, Stanford, CA 94309

March 1995

Prepared for the Department of Energy
under contract number DE-AC03-76SF00515

Printed in the United States of America. Available from the National Technical Information Service, U.S. Department of Commerce, 5285 Port Royal Road, Springfield, Virginia 22161.

•Ph.D thesis, Tohoku University

Abstract

We have studied the differences in properties between quark and gluon jets using 3-jet events in hadronic decays of Z^0 bosons collected by the SLD experiment at SLAC. Gluon jets were identified in 3-jet events containing one jet tagged as a heavy quark jet. The tagged gluon jets were compared with a mixed sample of light quark(u, d and s) and gluon jets, and also with a mixed sample of heavy quark (c and b) and gluon jets. Our study shows that the particle multiplicity of gluon jets is higher than that of light quark or heavy quark jets. The ratios of average charged multiplicities of gluon and quark jets are measured to be

$$\frac{\langle n_{gluon}\rangle}{\langle n_{quark}^{light}\rangle} = 1.29 \pm 0.06(\text{stat.})^{+0.05}_{-0.06}(\text{syst.}) \ ,$$

$$\frac{\langle n_{gluon}\rangle}{\langle n_{quark}^{heavy}\rangle} = 1.18 \pm 0.06(\text{stat.})^{+0.07}_{-0.04}(\text{syst.}) \ .$$

These results are in quantitative agreement with QCD model expectations. Differences are also observed in particle energy spectra and jet widths, consistent with naive QCD expectations. The experimental results are compared to Monte Carlo models of the hadronization process.

Acknowledgements

First, I would like to thank the SLC/SLD collaboration for the successful construction and operation of the experiment.

I would like to thank Professor Haruo Yuta for his guidance as my thesis advisor.

And I would also like to thank Professor Koya Abe, who gave me the start of the analysis.

In particular I would like to thank Phil Burrows for the many insightful discussions and his encouragement. And thanks to the QCD group, Dave Muller, Mike Strauss, Hiro Masuda, Takashi Maruyama, Mike Hildreth, Tom Junk, Jingchen Zhou and many others.

I would especially like to thank my fellows, Takashi Akagi, Kazushi Neichi, Yoji Hasegawa, and Yukiyoshi Ohnishi for the discussions about physics and life in general.

Many thanks to the whole SLD Tohoku group, Fumihiko Suekane, Tadashi Nagamine, Shinya Narita, Haruhiko Araki, Kazumi Hasuko, Yoshinori Takahashi, Gou Shishido, and to the Nagoya group, Ryoichi Kajikawa, Shiro Suzuki, Akira Sugiyama.

I thank my friends at Tohoku, Kyoko Tamae, Yumi Suzuki, Masao Kuriki, Takayuki Matsumoto, Syuichiro Hatakeyama, Hiroyuki Kawasaki, Masayuki Koga, Kou Fujita, Atsushi Iwasaki, Masahiro Onoda, Osamu Watanabe, Jun Yashima, Masatoshi Ishikawa, Kouki Kawamorita, Takasumi Maruyama, Akihiro Kaga, Takashi Kanno, Tetsuya Kinebuchi, Kouichi Kino, Kouji Maeda, Fuhito Nakanishi, Kaori Nanba, Mizuki Saitou, Toshikiyo Tanaka, and Kenichi Takeuchi.

And finally, I thank my wife Yasuko and my family for their support and encouragement.

Contents

List of Tables

List of Figures

LIST OF FIGURES

Chapter 1

Introduction

Quantum Chromodynamics, QCD, is a non-Abelian local gauge invariant field theory which describes the strong interactions between colored quarks and gluons. It is a fundamental element in the standard model of the known interactions(except gravity) of elementary particles. QCD was developed as an analogy of QED(Quantum Electrodynamics). QED provides accurate theoretical predictions which have been tested by experiments with high precision. On the contrary, QCD tests are rather less precise due to the complexity of physical properties involved in QCD: asymptotic freedom and color confinement. Asymptotic freedom means that the effective strong coupling constant decreases logarithmically at short distances so that we can apply perturbation theory to QCD in large momentum transfers. However, the strong coupling constant is still large enough so that the higher order corrections, which could give significant shifts to current theoretical predictions, are not calculable with high precision even in the large momentum transfer regime. Color confinement means that the potential energy between color charges increases approximately linearly at large distances, so that quarks are confined in hadrons. Therefore, we can not observe bare quarks and gluons, the elementary fields of QCD, but can observe colorless bound states of these constituents, hadrons.

From these reasons, it is very hard to derive properties of the quark-gluon interactions

from the hadronic states. QCD analysis of high energy experiments are done in the framework of the QCD-improved parton models. In other words, we have to use some models with perturbative QCD approximation, QCD-improved parton models, to extract basic features of QCD from the hadronic final states which we observe. As a consequence of such difficulties in QCD measurements, not only single experiment but many experiments are required to test qualitative QCD predictions and QCD models.

A comparison of quark and gluon jet properties is one of the long-standing difficult problems in QCD. This is due to the difficulty of gluon jet identification on the experimental side and the difficulty of subasymptotic corrections on the theoretical side. Lowest order QCD predicts 9/4 for the multiplicity ratio of gluon to quark jets. This value is expected from the color charge ratio of gluon($C_A = 3$) to quark($C_F = 4/3$). For quark and gluon jets with equal energy, this multiplicity ratio implies that gluon jets have a softer particle energy spectrum compared with quark jets. We can also expect that the angular distribution of particles relative to the jet axis in gluon jets is wider than that in quark jets because the mean transverse energy of the particles is about the same. However, these naive expectations are substantially reduced due to higher order corrections. The multiplicity ratio of hadrons in quark and gluon jets, for instance, is corrected to 1.38 ± 0.02 in a recent QCD calculation with a hadronization model[1].

Experimental searches for the differences between quark and gluon jets have been performed in the experiments of e^+e^- and $\bar{p}p$ collisions, and some indications of quark and gluon jet differences were reported[2, 3]. However, some of their analyses based on the comparison of quark jets from one experiment and gluon jets from other experiment, and relied on Monte Carlo simulations. Thus, their results were indirect, and would be biased by the different experimental environments and by the choice of the Monte Carlo simulations. Recently, analyses with high statistics data were performed by the LEP experiment[4, 5, 6]. They performed the direct comparison using symmetric 3-jet events in Z^0 hadronic decays and reported significant differences.

In order to search for the differences between quark and gluon jets, we have performed

a measurement using Z^0 hadronic decay data collected by the SLC Large Detector(SLD) experiment at SLAC[1]. About 250 members from 34 institutions collaborate on the SLD experiment[2]. The SLAC Linear Collider(SLC) is the first e^+e^- linear collider successfully operated at the Z^0 peak, and produces Z^0 events with the small and stable Z^0 production point. The SLD with its precise vertex detector has excellent efficiency for separating heavy hadrons' secondary vertices from the primary vertex. These SLC/SLD features and our analysis method allow efficient flavour tagging of jets in Z^0 hadronic events with high purity, and make the gluon jet analysis possible even with smaller data sample than the LEP experiments. The efficient flavour tagging of jets in this experiment is one of the motivations for this study. The first engineering run was carried out in 1991, the physics run started in 1992 and data are still being taken. This thesis is based on about 63,000 Z^0 hadronic decay data taken in 1992 and 1993 runs.

The content of this thesis is organized as follows. In chapter 2, some foundations of QCD relevant to this study are reviewed. Experimental apparatus is described in chapter 3. In chapter 4 the details of the event and track selection procedures are presented. The analysis method and the results are presented in chapter 5. Finally, the conclusion is given in chapter 6. In appendices, Monte Carlo models of hadronization process are compared to the experimental results, and the systemtic errors are discussed.

[1]Stanford Linear Accelerator Center

[2]The institutions and the members of the SLD collaboration are listed in Appendix A

Chapter 2

Theoretical Backgrounds

In this chapter, we review the decay of Z^0 gauge bosons produced by e^+e^- annihilation which provides us an excellent experimental environment to study QCD. Then, some foundations of QCD relevant to this study are outlined, and the differences between quark and gluon jets are discussed with the experimental measurements. As described in chapter 1, experimental QCD studies have to employ some phenomenological QCD models for the parton evolution and the hadronization process. Thus, we give a brief explanation of the models used in this analysis.

2.1 Production and Decay of Z^0 Gauge Bosons

The fundamental process of electron-positron annihilation is $e^+e^- \rightarrow f\bar{f}$, where $f = e, \mu, \tau, \nu_e, \nu_\mu, \nu_\tau, u, d, s, c, b$ at the Z^0 mass energy. There are two basic neutral gauge bosons which contribute to this process: the photon and the Z^0. The Feynman diagrams of the lowest order electron-position annihilation(except for $e^+e^- \rightarrow e^+e^-$) are shown in Fig. 2.1. The cross section, σ, of $e^+e^- \rightarrow f\bar{f}$ at the center of mass energy, $\sqrt{s}$, close to the mass of Z^0, M_Z, is proportional to square of the sum of matrix elements of two diagrams, $|\mathcal{M}_\gamma + \mathcal{M}_Z|^2$: a pure electro-magnetic interaction term, a pure weak interaction term and an interference term of the two interactions. At $\sqrt{s} = M_Z$, the interference term vanishes.

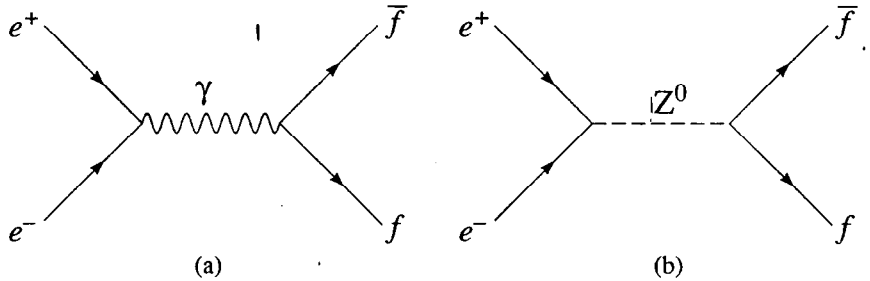

Figure 2.1: The fundamental processes of $e^+e^- \to f\bar{f}$.

Therefore, the weak interaction dominates because the electro-magnetic interaction is small at the Z^0 pole. ($\sigma_{weak}/\sigma_{em} \sim 1100$). In this case, the lowest order differential cross section at the Z^0 mass energy is written in a simple form[7] by neglecting the initial and final state fermion masses as

$$\frac{d\sigma}{d\cos\theta} = \frac{\pi\alpha^2}{2}\frac{s}{(s-M_Z^2)^2+\Gamma_Z^2M_Z^2}[(v_e^2+a_e^2)(v_f^2+a_f^2)] \times\left[1+\cos^2\theta+8\cos\theta\frac{v_ea_e}{v_e^2+a_e^2}\frac{v_fa_f}{v_f^2+a_f^2}\right], \quad (2.1)$$

where M_Z and Γ_Z are the mass and total decay width of Z^0, θ is the angle between the initial electron and final fermion, α is the fine structure constant. v_e, a_e, v_f and a_f are the vector and axial vector couplings to Z^0 gauge boson for electron and fermion, respectively. The Z^0 mass, width and branching ratio to each fermion pair are listed in Table 2.1[8].

2.2 Quantum Chromodynamics

Since the discovery of the π meson in 1947, a large collection of hadron mass spectra and hadronic interactions in high energy experiments strongly suggested that there exist point-like structures within hadrons. In 1968, the deep inelastic electron-proton scattering experiment at SLAC observed the first direct evidence for quarks, which carry roughly one third of the nucleon energy. In 1972, QCD[9, 10, 11] was born in the form of a simple and elegant

Z^0 mass(M_Z)	91.187	±	0.007	GeV/c^2
Z^0 decay full width(Γ_Z)	2.490	±	0.007	GeV
Z^0 decay branching fractions				
e^+e^-	(3.366	±	0.008	)%
$\mu^+\mu^-$	(3.367	±	0.013	)%
$\tau^+\tau^-$	(3.360	±	0.015	)%
invisible	(20.01	±	0.16	)%
hadrons	(69.90	±	0.15	)%
$(u\bar{u}+c\bar{c})/2$	(9.7	±	1.8	)%
$(d\bar{d}+s\bar{s}+b\bar{b})/3$	(16.8	±	1.2	)%
$c\bar{c}$	(11.9	±	1.4	)%
$b\bar{b}$	(15.45	±	0.21	)%

Table 2.1: Z^0 properties.

Flavour	I	I_3	S	C	B	T	Q/e	mass
d	1/2	−1/2	0	0	0	0	−1/3	5 to 15 MeV/c^2
u	1/2	1/2	0	0	0	0	+2/3	2 to 8 MeV/c^2
s	0	0	−1	0	0	0	−1/3	100 to 300 MeV/c^2
c	0	0	0	1	0	0	+2/3	1.0 to 1.6 GeV/c^2
b	0	0	0	0	−1	0	−1/3	4.1 to 4.5 GeV/c^2
t	0	0	0	0	0	1	+2/3	$174 \pm 10^{+13}_{-12}$ GeV/c^2

Table 2.2: Quark summary. Top quark mass is from a CDF observation of top candidate events. B indicates quantum numbers of bottomness, not baryon numbers.

Lagrangian based on the gauge group $SU(3)_{color}$. In 1974, a new particle, the J/ψ, was discovered at SLAC and Brookhaven simultaneously, and was interpreted as a bound state of $c\bar{c}$. Subsequently, the Υ was discovered at FNAL in 1977, which is a bound state of $b\bar{b}$, a bottom quark and an anti-bottom quark. After the discovery of charm and bottom quarks, our quark table(Table 2.2) has enlarged.

Five quark flavours out of six flavours have been found experimentally. The top quark (sixth quark) has been suggested to exist at 150~180 GeV by the radiative corrections of higher order weak interactions[8]. Recently, the CDF collaboration has observed a possible signal of the top quark[12]. Quarks are spin 1/2 fermions with fractional charges of $+\frac{2}{3}e$ for up type quark(u, c, t) and $-\frac{1}{3}e$ for down type quarks(d, s, b). Quarks can carry one of three strong charges, called color charges, say Red, Blue or Green conventionally. Anti-quarks can carry the corresponding anti-color. The color symmetry is supposed to be exact, thus the strong interaction is independent of colors. The boson intermediating strong interaction between quarks is named the gluon. The gluon is a spin 1 massless boson and carrys a color and an anti-color or their combinations$(R\bar{B}, R\bar{G}, B\bar{G}, B\bar{R}, G\bar{R}, G\bar{B}, \frac{1}{\sqrt{2}}(R\bar{R}-B\bar{B}), \frac{1}{\sqrt{6}}(R\bar{R}+B\bar{B}-2G\bar{G}))$. The color charge in strong interactions is analogous to the electric charge in electromagnetic interactions. In both interactions, a massless spin 1 boson(a photon or a

gluon) mediates the force. The important difference between them is that photons have no charge, while gluons have. Therefore, gluons can interact with other gluons, whereas photons can not interact with each other. The existence of this direct coupling of gluons differentiates the charge screening of QCD from that of QED. The resulting "anti-screening" of the color is referred to as "asymptotic freedom". This means that the strength of the interaction between quarks decreases as the distance between them decreases, and the state of quarks approaches to be free asymptotically. This behavior allows us to use perturbative QCD calculation for short distances. On the contrary, at long distances, quarks interact strongly and so can never escape. This is, called "confinement of quarks(and gluons)", corresponding to the hadronic states. Perturbation theory is not applicable for the hadronization process of quark and gluons because the coupling is so strong. Thus, we have to use phenomenological models to describe such states.

2.3 Quark and Gluon Jet Differences

In QCD, gluons are massless, spin 1 bosons with color charge which should be 9/4 times as large as that of quarks. In this section, we briefly review the quark and gluon jet differences in terms of particle multiplicities in jets.

The color charge of the quark, C_F, is 4/3 and that of the gluon, C_G, is 3. This means that the three-gluon coupling, which determines the properties of gluon jets, is stronger than the qqg coupling relevant to quark jets. Therefore, we can naively expect that the multiplicity in gluon jets is higher than that in quark jets. Correspondingly, the energy spectrum of particles in gluon jets is expected to be softer than that in quark jets. The distribution of the angle between the particle and the jet axis in gluon jets is also expected to be wider than that in quark jets because the mean transverse energy of gluon radiation in both jets is expected to be about the same.

The multiplicity ratio, R, of gluon jets to quark jets is given as the ratio of color charges

in the lowest order QCD prediction,

$$R = C_G/C_F = 9/4. \tag{2.2}$$

This lowest order R value is not too small to be observed experimentally. When higher order corrections are taken into account[13], however, this ratio is reduced to

$$R = \frac{9}{4}[1 - 0.27\sqrt{\alpha_s} - 0.07\alpha_s]. \tag{2.3}$$

Recently, R was calculated by using the exact solution of QCD equations for generating functions with fixed coupling[1]. The ratio of parton(see Chapter 2.4) multiplicities is predicted to be

$$R_{\rm parton} = 1.84 \pm 0.02. \tag{2.4}$$

By the use of the HERWIG Monte Carlo simulation[14], $R_{\rm parton}$ is related to the hadronic ratio $R_{\rm hadron}$ which can be measured by experiments

$$\begin{aligned} R_{\rm hadron} &= R_{\rm parton}\frac{R^{\rm MC}_{\rm hadron}}{R^{\rm MC}_{\rm parton}} \\ &= 1.38 \pm 0.02, \end{aligned} \tag{2.5}$$

where $R^{\rm MC}_{\rm parton}$ and $R^{\rm MC}_{\rm hadron}$ are the ratios for partons and hadrons in the Monte Carlo, respectively. Thus, R is significantly reduced by the hadronization process in the prediction.

Experimentally the HRS collaboration has measured the ratio of charged multiplicities R_{ch} with symmetric 3-jet events in e^+e^- annihilation at PEP[3]. In the analysis, the symmetric 3-jet events were collected in which all jets were produced with a relative angle of 120 degrees in the event plane and had the same jet energies $E_{jet} = \sqrt{s}/3$. Thus, the probability of a jet originating from a gluon is the same for each jet in the event. From Monte Carlo simulations, they estimated that the charged multiplicity of quark jets at $\sqrt{s} = 2E_{jet}$ is 5.2. To obtain the charged multiplicity of gluon jets, a model with Poissonian multiplicity distribution is assumed. The model reproduces the measurement with the charged multiplicity of gluon jets equal to $6.7^{+1.1}_{-2.1} \pm 1.0$. Therefore, the charged multiplicity ratio R_{ch} is $1.29^{+0.21}_{-0.41} \pm 0.20$, indicating no significant difference in the charged multiplicity between quark and gluon jets within the quoted error.

The OPAL, DELPHI, and SLD collaborations have measured the ratios of multiplicities, energy spectra and jet widths using different type of symmetric 3-jet events in Z^0 hadronic decays[5, 6, 15]. They select the symmetric 3-jet events, in which the angles from the highest energy jet to other two jets are the same. In such an event configuration, the highest energy jet is a quark jet with high probability. Thus the two lower energy jets are a quark and a gluon jets. If one of the two jets is tagged as a heavy quark jet, then the remaining jet is anti-tagged as a gluon jet. The multiplicity ratios measured by OPAL are

$$\begin{aligned} R &= 1.267 \pm 0.043 \pm 0.055 \quad : E_{jet} = 24\text{GeV}, \\ R_{ch} &= 1.326 \pm 0.054 \pm 0.073 \quad : E_{jet} = 24\text{GeV}. \end{aligned} \tag{2.6}$$

where R_{ch} is the ratio of the charged multiplicities. The DELPHI collaboration has measured

$$\begin{aligned} R &= 1.22 \pm 0.04 \quad : E_{jet} = 30\text{GeV}, \\ R &= 1.172 \pm 0.032 \quad : 15 < E_{jet} < 39\text{GeV}. \end{aligned} \tag{2.7}$$

All the values are significantly larger than unity, indicating that the multiplicity of gluon jets is larger than that of quark jets. However, the ratios R are somewhat smaller than the prediction given by eq. 2.5. The preliminary result measured by the SLD collaboration is

$$R_{ch}^{gluon/light\,quark} = 1.36 \pm 0.24 \quad : E_{jet} = 24\text{GeV}. \tag{2.8}$$

This is the charged multiplicity ratio of gluon to light quark jets. Thus, we can not compare this value with the OPAL and the DELPHI results directly.

2.4 QCD Models in e^+e^- Annihilation

The evolution of hadron jet in e^+e^- annihilation takes place in four phases by means of the interactions and models, as shown in Fig. 2.2. In the first phase, the initial e^+e^- pair annihilates into a gauge boson, a photon or a Z^0, which in turn decays into a quasi free pair of quark and anti-quark. This process is well described by electro-weak theory, as explained

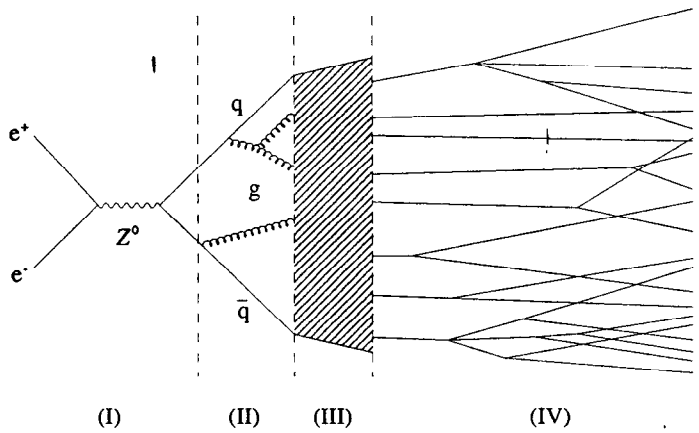

Figure 2.2: Schematic illustration of $e^+e^- \rightarrow$ hadrons.

in section 2.1. In the second phase, QCD plays an important role, and thus the differences between quark and gluon jets are caused. Gluons are radiated from initial quarks, and in turn gluons may radiate gluons, or create quark antiquark pairs. The quarks and gluons in this phase are called "partons". In principle, there are two approaches for calculating parton configurations[16, 17]: Matrix Element(ME) and Parton Shower(PS) methods. The ME is the exact QCD matrix elements that has been calculated up to second order($\mathcal{O}(\alpha_s^2)$, up to 4-parton production). The PS is the leading logarithmic approximation of QCD, and is formulated as a branching process of virtual partons according to the Altarelli-Parisi equations[18]. In the third phase, hadrons are generated from partons. This phase can not yet be calculated in QCD, as described in chapter 1. Thus, phenomenological parameterization of hadron production must be used to describe this phase in Monte Carlo simulations. In the last phase, hadrons decay into stable hadrons and leptons, which can be observed by experiments. In the following sections, we review the QCD models used in the second and third phase.

2.4.1 The Matrix Element Method

The standard approach of calculating the hadronic cross section is the Matrix Element method in which we calculate the amplitude of Feynman diagrams up to a fixed order of α_s. To get the rate of N-parton production, the matrix elements are added and squared, then integrated over the phase space. According to the N-parton fraction determined by the matrix elements, the multiplicity of partons and 4-momentum of partons are determined in a Monte Carlo simulation.

The first order QCD correction to $e^+e^- \rightarrow q\bar{q}$ is the gluon radiation from the q or $\bar{q}$. The differential cross section for this configuration($e^+e^- \rightarrow q\bar{q}g$, 3-parton) is calculated[19] for massless quarks as

$$\frac{d\sigma}{dx_1 dx_2} = \sigma_0 \frac{\alpha_s}{\pi} \frac{2}{3} \frac{x_1^2 + x_2^2}{(1-x_1)(1-x_2)}, \tag{2.9}$$

where σ_0 is the cross section for $e^+e^- \rightarrow q\bar{q}$, x_1, x_2 and x_3 are the scaled energy variables in the CM frame of the event

$$\begin{aligned} x_1 &= 2E_q \ /\sqrt{s}, \\ x_2 &= 2E_{\bar{q}} \ /\sqrt{s}, \\ x_3 &= 2E_g \ /\sqrt{s}. \end{aligned} \tag{2.10}$$

The kinematically allowed region is $0 \leq x_i \leq 1 (i=1,2,3)$. For x_1 or $x_2 \rightarrow 1$, the cross section for 3-parton(eq. 2.9) diverges. However, the divergence is canceled when the first order propagator and vertex corrections are taken into account. This cancellation corresponds to a difficulty to distinguish a gluon from a quark which is soft or collinear to the quark. In a Monte Carlo, the divergence is solved by a cut-off mass of two partons(a quark and a gluon):a gluon is radiated if the virtual mass of the gluon and quark is larger than a certain cut-off mass. In other words, events with a hard gluon are generated according to the cross section in eq. 2.9, but events with a soft or collinear gluon are combined to 2-parton events.

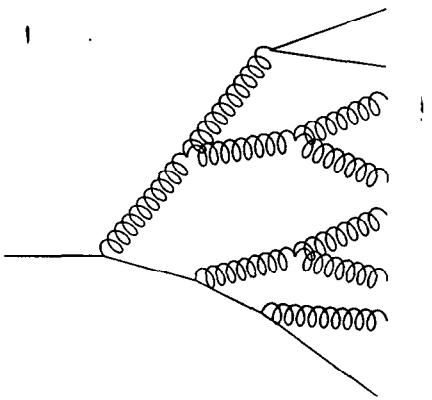

Figure 2.3: Schematic illustration of a parton shower. Lines and spirals represent quarks(or anti-quarks) and gluons, respectively.

In second order QCD, two new parton configurations are added to the first order configurations:$e^+e^- \to q\bar{q}gg$ and $e^+e^- \to q\bar{q}q'\bar{q}'$. The cross section of 4-parton events has been calculated by several groups[20]. The same rules as 3-parton calculations can be applied to 4-parton configuration. As in the 3-parton case, divergences appear, but are removed by the cut-off mass.

2.4.2 The Parton Shower Method

The Parton Shower method(PS) is based on the leading-log approximation of perturbative QCD. The initial quarks are produced with off-shell mass, and decay(or branch) into virtual partons which in turn decay(Fig. 2.3). Progressive branchings continue until they reach a certain cut-off mass Q_0. In this method, only the leading logarithmic terms in the perturbative QCD expansion of the two body decay cross section are used. The basic branchings are

$$\begin{aligned} q &\to q+g, \\ g &\to g+g, \\ g &\to q+\bar{q} \end{aligned} \tag{2.11}$$

where $q(\bar{q})$ and g represent a quark(anti-quark) and a gluon, respectively. The Altarelli-Parisi splitting kernels for the parton branchings[18] are

$$\begin{aligned} P_{q\to q+g} &= C_F\left(\frac{1+z^2}{1-z}\right), \\ P_{g\to g+g} &= \frac{2C_G(1-z+z^2)}{z(1-z)}, \\ P_{g\to q+\bar{q}} &= T_R(z^2+(1-z)^2), \end{aligned} \tag{2.12}$$

where C_F and C_G are the color charges of quark(4/3) and gluon(3) respectively, and $T_R = N_f/2$, where N_f is the available number of quark flavours for quark pair creation. The probability distribution for this branching is given by

$$\frac{dP_{a\to b+c}}{dt} = \int dz \frac{\alpha_s(Q^2)}{2\pi} P_{a\to b+c}(z) \tag{2.13}$$

where t is the evolution parameter($t = \ln(Q^2/\Lambda^2)$) and z specifies the fraction of four-momentum for daughter b. In this model, no interference between branchings is taken into account. The PS Monte Carlo has only two parameters:the leading-log QCD scale Λ and the cut-off mass Q_0. An advantage of the PS compared to the ME is that we can generate more than 4 partons, which is the current limit of number of partons generated by the ME. The maximum number of partons in the PS is determined by the cut-off mass Q_0.

2.4.3 Color Dipole Model

In the case of e^+e^- annihilation, perturbative QCD can be formulated in an alternative in terms of quarks and gluons or in terms of color dipoles. The Color Dipole Model(CDM)[24,

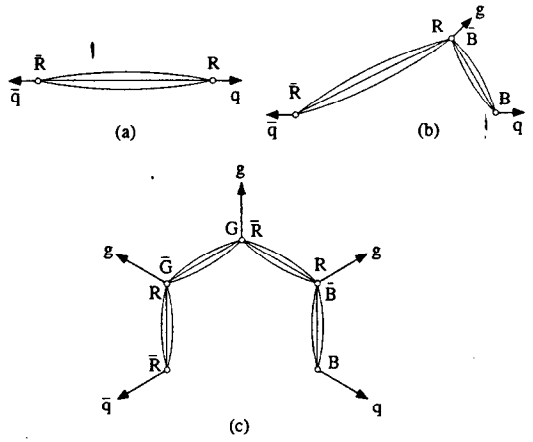

Figure 2.4: Schematic illustration of the color dipole model.

25] is based on the fact that an emission of a gluon from a $q\bar{q}$ pair can be treated as a radiation from the color dipole between quark and anti-quark(Fig. 2.4(a) and (b)). The emission of a second gluon is treated as radiation from two independent dipoles: one stretched from the quark to the gluon and the other from the gluon to the anti-quark(Fig. 2.4(b)). This process is generalized so that one more gluon is given by three independent dipoles, etc(Fig. 2.4(c)).

There are three different types of dipole:the dipoles between a quark and an antiquark, between a quark and a gluon, and between two gluons. The cross section for gluon emission from the dipoles are calculated[23] as

$$\begin{aligned} q\bar{q} &\to q\bar{q}g &: \frac{d\sigma}{dx_1 dx_3} &= \sigma \frac{2\alpha_s}{3\pi} \frac{x_1^2 + x_3^2}{(1-x_1)(1-x_3)}, \\ qg &\to qgg &: \frac{d\sigma}{dx_1 dx_3} &= \sigma \frac{3\alpha_s}{4\pi} \frac{x_1^3 + x_3^2}{(1-x_1)(1-x_3)}, \\ gg &\to ggg &: \frac{d\sigma}{dx_1 dx_3} &= \sigma \frac{3\alpha_s}{4\pi} \frac{x_1^3 + x_3^3}{(1-x_1)(1-x_3)}, \end{aligned} \tag{2.14}$$

where x_i are the final state energy fractions, $2E_i/\sqrt{s_{dip}}$, of the emitting partons in the center of mass system of the dipoles.

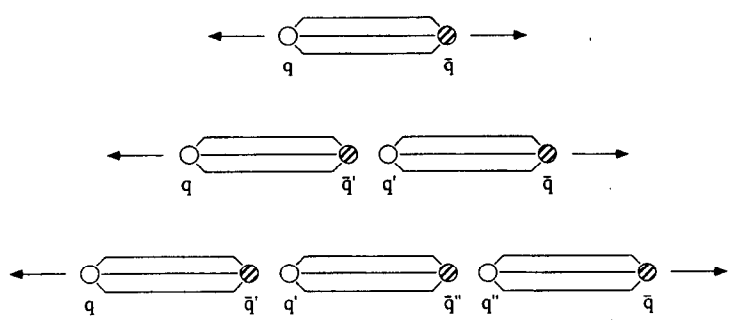

Figure 2.5: Schematic illustration of the string fragmentation model.

2.5 Hadronization Models

In this section, two conventional hadronization models relevant to this study will be reviewed:the String Fragmentation(SF) and Cluster Fragmentation(CF) models. In the SF, the color confinement is a basic concept: hadrons are produced from colorless string systems, not from isolated colored quarks. In the CF, hadronization process is described by massive colorless objects like the SF. But important difference between the CF and the SF is that no assumptions of fragmentation functions of partons are needed in the CF as a result of colorless clusters.

2.5.1 String Fragmentation Model

The String Fragmentation(SF) model is implemented in the JETSET Monte Carlo program[21]. The string model for $q\bar{q}$ system is basically a simple color confinement picture for hadronization. The main assumption of the SF model is that the fragmentation of outgoing partons are not independent. In the SF, a virtual string is considered to be a color flux tube be-

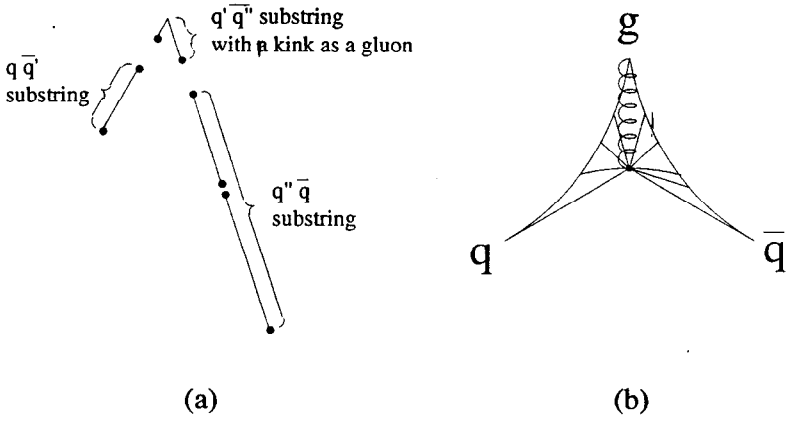

Figure 2.6: Gluon radiation in the string model:(a)a kink of a string. (b)virtual strings in the CMS.

tween partons(Fig. 2.5). The transverse dimension of the tube is roughly 1 fm. As the partons move apart, the string is stretched. Thus, the potential energy stored in the string is increased and the string may break by a new $q'\bar{q}'$ pair creation. In this manner the initial state $q\bar{q}$ system splits into two color singlet systems, $q\bar{q}'$ and $q'\bar{q}$. This string stretching and breaking process may occur until invariant masses of $q\bar{q}$ are small enough. After this process, hadrons are formed by the quark from one break and the anti-quark from adjacent break.

When the $q'\bar{q}'$ pair is created by the breaking of the string, transverse momenta are give to q' and $\bar{q}'$. The production probability is proportional to

$$\exp(-\pi m_T^2/\kappa) = \exp(-\pi m^2/\kappa)\exp(-\pi P_T^2/\kappa), \tag{2.15}$$

where m_T is called transverse mass, m_q is the virtual mass of the newly created quark, and P_T is the transverse momentum. The default value of P_T in JETSET is 0.40 GeV. Eq. 2.15 also gives relative rates for the production of quark flavour on the basis of quark mass(u:d:s:c $\approx 1{:}1{:}0.3{:}10^{-11}$).

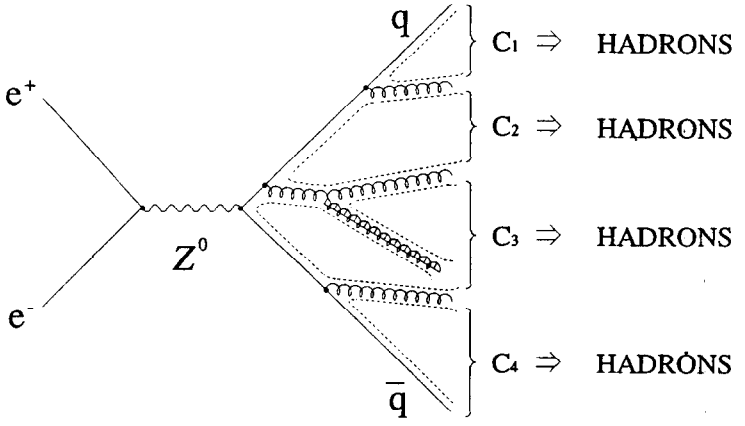

Figure 2.7: Schematic illustration of cluster model. Dotted lines represent color flows.

The longitudinal fragmentation is formulated in terms of a probability distribution $f(z)$. z is the fraction of the energy given by the initial $q\bar{q}$ pair to the newly created hadron. In JETSET,

$$f(z) \sim \frac{1}{z}(1-z)^a \exp(\frac{-bm_T^2}{z}) \tag{2.16}$$

is used with the parameter value $a = 1$ and $b = 0.7$.

In the SF model, gluons correspond to kinks on the string spanned between a quark and an antiquark. Thus, a gluon has two string pieces attached to it, while a quark or an antiquark has one string(Fig. 2.6).

2.5.2 Cluster Fragmentation Model

The first Cluster Fragmentation(CF) model was presented by Field and Wolfram[22]. In the CF model, hard color separations are neutralized before hadrons are actually formed. This color screening process is interpreted as the initial state is evolved into a collection of low mass colorless clusters. So the role of the QCD dynamics is limited to describing

the production of this final cluster states. In this model, no assumptions of fragmentation functions of partons are used. This is the important difference between the CF and the SF model described in previous section.

After the parton shower is generated from initial quarks, final-state partons are put on mass shell. Then final-state gluons are split into $q\bar{q}$ pairs

$$g[p] \rightarrow q[zp] + \bar{q}[(1-z)p], \tag{2.17}$$

where g and q represent a gluon and a quark with 4-momentum p and zp. Several choice were tried for the probability function of z. In this process, color flows between partons are formed(dotted lines in Fig. 2.7), and the color charge is assigned to quark(Fig. 2.7). Then final state quarks are linked to a unique parton partner, anti-quark, by the color charge information, and form clusters. The clusters have a mass M and quark flavours of q and $\bar{q}$. These clusters are then simply decayed into two hadrons

$$C_i(M, q_a, \bar{q}_b) \rightarrow H_1 + H_2, \tag{2.18}$$

where C_i and H represent a cluster and a hadron. The probability of the decay is given by

$$P(C_i \rightarrow H_1 + H_2) = P_F \cdot P_S \cdot P_K \tag{2.19}$$

where P_S is the number of spin state of final hadrons, P_K is a 2-body phase space suppression factor and P_F is an available flavour factor of final hadrons. The decay mode is chosen from all possible decays at random with the individual flavor factor weight. Unstable hadrons produced in clusters are decayed subsequently until stable hadrons are produced.

Chapter 3

Experimental Apparatus

The data used in this analysis were collected by the SLC/SLD facility at the Stanford Linear Accelerator Center(SLAC). The SLAC Linear Collider(SLC) is the unique e^+e^- linear accelerator designed to produce the Z^0 boson and the first linear collider successfully operated in the world. The SLC Large Detector(SLD), replaced the Mark II detector in 1991, is a multi-purpose detector with full 4π coverage placed at the SLC's interaction point(IP). In the following sections, we describe the SLC/SLD that made our measurement possible.

3.1 SLC

The SLAC Linear Collider(SLC) is the first electron-positron linear collider(50 GeV×50 GeV) operated in the world. Electrons and positrons are accelerated in the 3 km-long linear accelerator(linac) simultaneously and collide at the interaction point(IP) to produce Z^0 bosons after being guided by arcs. The construction of SLC began in 1983 and was completed in 1987. The first Z^0 event was observed with the Mark II detector in April, 1989. Some of the great features of SLC are (1) longitudinally polarized electron beam and (2) the small beam size. Some basic SLC parameters are listed in Table 3.1.

A schematic of the SLC is shown in Fig. 3.1. At first, two bunches of electrons are

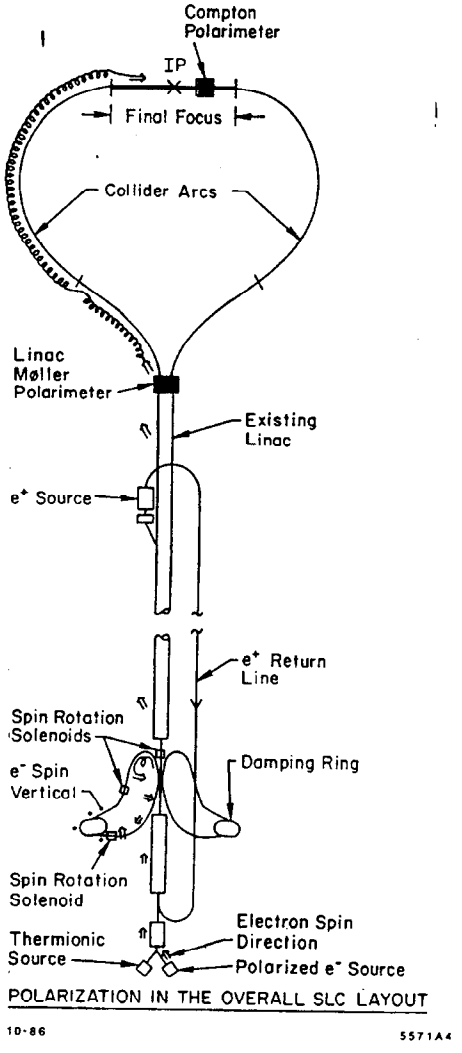

Figure 3.1: Schematic view of the SLC.

Year	1992	1993
E_{cm}	91.55 GeV	91.26 GeV
Electron polarization	22.4%	63.0%
Number of electrons/bunch	3.0×10^{10}	3.5×10^{10}
Number of positrons/bunch	3.0×10^{10}	3.5×10^{10}
Beam size	$2\mu m \times 2\mu m$	$2.3\mu m \times 0.8\mu m$
Bunch length	$1.2mm$	$0.6mm$

Table 3.1: The SLC beam parameters.

created by photoemission from a GaAs photocathode at the polarized electron source. Those bunches are accelerated to 0.2 GeV by the energy booster and to 1.0 GeV by a linac and are transported to the North Damping Ring. In the South Damping Ring, two bunches of positrons are accumulated(we describe positron creation later). In the damping rings, the emittance of each bunch is reduced. One bunch of positrons is extracted from the South Damping Ring and then injected into the linac. The pulse compressor reduces the bunch length from 1 cm to 1 mm. After the positron bunch, two bunch of electrons are also injected into the linac. The distance of those bunches are 17.6 m. First two bunches(positrons and electrons) are accelerated to 46.7 GeV before entering the South and North Arc, respectively. The last bunch of electrons is accelerated to 33 GeV, extracted from the linac and guided to a Tantalum-Tungsten target to produce positrons. In the target, positrons are produced by pair-creation from the bremsstrahlung of electrons, and are collected by a focusing solenoid. Positrons are transported back to the beginning of the linac by the Return Line, and then accelerated to 1.0 GeV to transported to the South Damping Ring. In the meantime, the first two bunches of positrons and electrons accelerated up to 46.7 GeV are split by a dipole magnet at the end of the linac and transported through the SLC arcs toward the interaction point. The bunches are focused in Final Focus System(FFS) to order of 1 μm of transverse size at the interaction point. The beams are crossed at the IP, and then the beams are kicked

into the extraction lines and led to the north and south beam damps.

3.1.1 Beam Energy Measurement

The beam energy spectrometers are located at the end of the beam transport system, 150 m past the IP, on the south arc for electrons and on the north arc for positrons. The beam energies of positrons and electrons are measured by bending the beams through three dipole magnets shown in Fig. 3.2. The deflection angle θ is related to the beam energy by the expression,

$$E_{beam} = \frac{c}{\theta} \int |dl \times \boldsymbol{B}| \tag{3.1}$$

where $\boldsymbol{B}$ is the magnetic filed of the analyzing magnets and dl is the path length in the analyzing magnet along the beam. The deflection angle is measured by the Wire Imaging Synchrotron Radiation Detector(WISRD)[26]. The first and third small magnets in Fig. 3.2 sweep the beam horizontally, creating parallel stripes of synchrotron radiation. The second magnet bends the beam down by 18.286 mrad. The distance between two stripes is measured by the WISRD 15 m away. The WISRD has two screens of copper wires which detect compton scattering of the electrons in the screens. During the 1992 and 1993 run, the average beam energies were 91.55 ± 0.04 GeV[27] and 91.26 ± 0.04 GeV[28], respectively.

3.2 SLD

The SLAC Large Detector(SLD)[29] is a general purpose detector optimized to measure Z^0 gauge boson produced by the SLC. The SLD was designed to provide 4π coverage detector for Z^0 physics. The SLD was designed in 1984 and the detector was completed in 1991. Its size is about 10 m×10 m×10 m. The SLD consists of several different purpose subsystems(refer to Fig. 3.3); tracking devices, calorimeters, particle identification devices and a magnet. The SLD subsystems are summarized in Table 3.2. To provide precision tracking

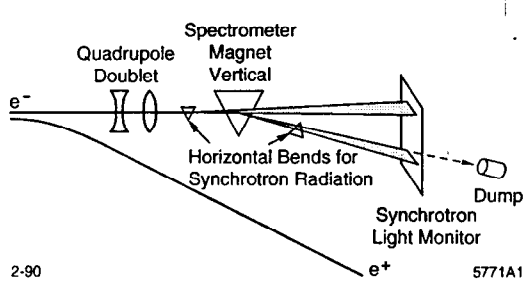

Figure 3.2: Schematic of the SLC beam-energy spectrometer.

of charged particles with 4π coverage, the SLD has a CCD vertex detector(VXD), a barrel drift chamber(Central Drift Chamber, CDC) and four Endcap Drift Chambers(EDC), located in 0.6 T magnetic field. The VXD and the CDC cover the barrel region, and the EDC(four endcap drift chambers) cover both the forward and backward endcap regions. The energy of particles is measured by three different sampling calorimeters, the silicon-tungsten calorimeter(LUM), the lead-liquid argon calorimeter(LAC) and the iron-streamer tube calorimeter(called the warm iron calorimeter, WIC). The LUM measures the luminosity of the SLC at the IP. The LAC measures electromagnetic and hadronic showers in both barrel and endcap regions. The WIC is used for additional measurement of hadronic shower, muon tracking and flux return of the magnetic field. Charged particle identification is made with the Cherenkov Ring Imaging Detector(CRID) for wide range of momentum.

The SLD uses spherical coordinates shown in Fig. 3.4. The polar angle θ is measured relative to the beam axis. The azimuthal angle ϕ describes rotations around the beam axis. The radial direction R describes a distance from the beam axis. In the right-handed cartesian coordinate system, z is defined to be along the positron beam axis. x coincides with $\phi = 0$ and y is perpendicular to x and z.

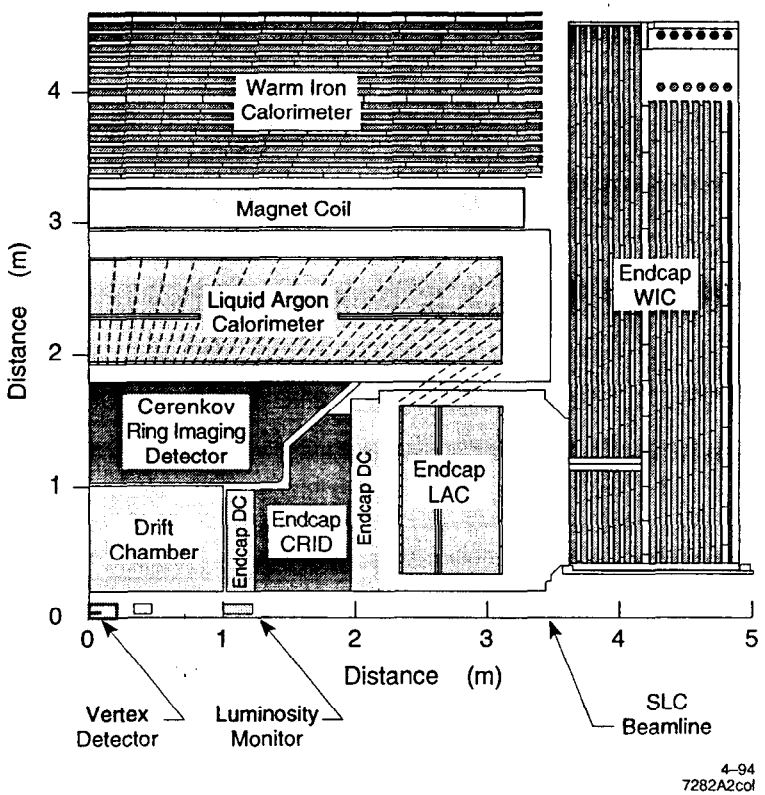

Figure 3.3: A quadrant schematic view of the SLD.

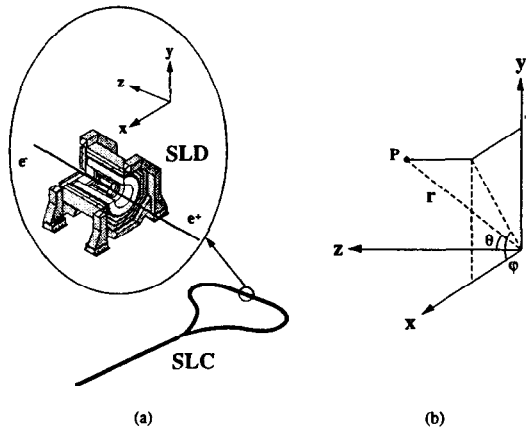

Figure 3.4: SLD coordinate system.

Tracking devices	
CCD Vertex Detector	barrel
Central Drift Chamber	barrel
Endcap Drift Chambers	endcap
Particle identification devices	
Cherenkov Ring Imaging Detector	barrel and endcap
Calorimeters	
Liquid Argon Calorimeter	barrel and endcap
Warm Iron Calorimeter	barrel and endcap
Luminosity Monitor and Small Angle Tagger	endcap
Medium Angle Silicon Calorimeter	endcap
Magnet	barrel

Table 3.2: SLD subsystems.

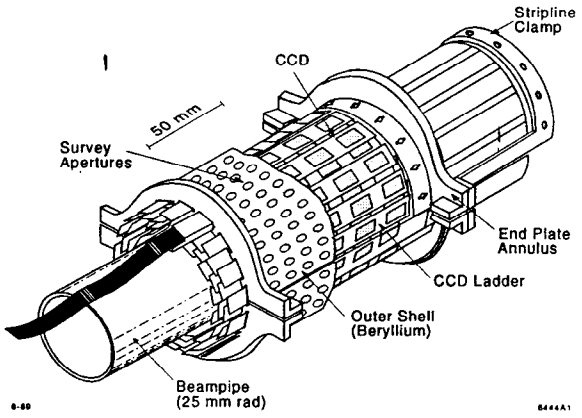

Figure 3.5: The CCD vertex detector.

3.2.1 CCD Vertex Detector

The Vertex Detector(VXD)[29, 30] is placed at the center of the SLD surrounding the IP. The VXD uses Charge Coupled Devices(CCDs) to measure the three dimensional positions of charged particles near the IP. The precise measurement near the IP improves the tracking resolution of the drift chamber and one can distinguish secondary vertices from the primary vertex(IP) in the decay of heavy particles with a relatively long lifetime .

The VXD uses semi-conductor device CCDs which provide three dimensional information of charged tracks. The CCD has 8.47 mm × 12.72 mm active area which is a matrix of 22 μm × 22 μm pixels, yielding an effective position resolution of $\sigma_{x,y} \sim 5\mu$m. Each pixel stores ionization information from charged particles that passed through it. The VXD contains 60 ladders, each ladder has 8 CCDs. The ladders are arranged in an overlapping fashion into four concentric layers of radii 29.5, 33.5, 37.5 and 41.5 mm around the 25.5 mm radius beampipe. The total thickness of the VXD, including the beampipe, is 5.82×10^{-2} radiation lengths. The VXD is cooled to $-80°$ C with nitrogen gas to reduce dark current and loss of CCD charged-transfer efficiency from radiation damage. The total readout time

Individual CCDs	
Pixel size	22 μm × 22μm
Active area	385 × 578 pixels(8.5 × 12.7 mm^2)
Total number of pixels	222,530
Min-I signal	1300 electrons(Landau peak)
Efficiency for min-I particles	$\geq$ 98%
Cluster size	80% of charge deposited in 1 to 2 pixels
Complete Detector	
Number of ladders	60
Total number of pixels	107 Mpixels
Radii of four layers	29.5, 33.5, 37.5, 41.5 cm
Readout time	152 ms(19 beam crossings)
Spatial resolution(xy)	5.5 μm
Spatial resolution(rz)	5.5 μm

Table 3.3: The CCD vertex detector parameters.

for the VXD is 152 ms, or 19 beam crossings at 120 Hz. Some basic VXD parameters are listed in Table 3.3.

3.2.2 Central Drift Chamber

The Central Drift Chamber(CDC) is a tracking device for charged particles covering the barrel region. Its shape is a cylindrical annulus, 2 m long with an inner radius of 0.2 m and an outer radius of 1.0 m. This volume is filled with a gaseous mixture of CO_2 92% and Isobutane 8%. The CDC contains 60 cells grouped in 10 concentric supper layers(Fig. 3.6. In order to measure z positions of charged tracks in the CDC, four of ten super layers are paralleled to the beam axis and six super layers are angled at $\pm$41 mrad with respect to the beam axis. Fig. 3.7 shows the configuration of a cell. Each cell has 27 field wires, 8 sense wires

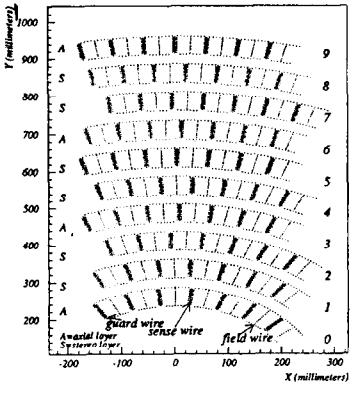

Figure 3.6: CDC superlayers.

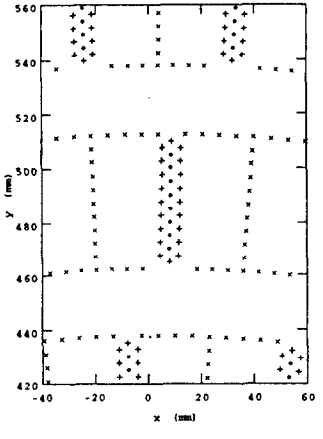

Figure 3.7: Detail of a CDC cell. • represents a sense wire. + and × represent a guard wire and a field wire, respectively.

Inner/outer radius	200/1000 mm
Length	2000 mm
Innermost/outermost wire layer radius	238/961 mm
Wire length	1800 mm
Number of superlayers	10
Number of axial/stereo superlayers	4/6
Number of cells	640
Number of sense wires per cell	8
Stereo angle	± 41 mrad
Sense wire diameter (tungsten)	25 μm
Field wire diameter (Cu-Be)	152 μm
Guard wire diameter (Cu-Be)	152 μm
Average drift field	0.13 kV/mm
Gas	CO_2 92%-Isobutane 8%
Average drift velocity	9 μm/ns
Amount of material:	
Inner wall	0.009 X_0
Wires	0.020 X_0
Gas	0.006 X_0
Outer wall	0.018 X_0
End plates and electronics	0.20 X_0

Table 3.4: The CDC parameters.

and 24 guard wires. The sense wires are made of tungsten, 25 μm radius and the resistance is 300 Ω. The field and guard wires are made of Cu-Be with 152 μm radius. The guard wires are surrounding the sense wires to shape electric fields. High voltages are applied to the field and guard wires to make electric fields. The charged particle passing through a cell creates electrons liberated by ionizing the gas. The liberated electrons drift in the electric field(0.13 kV/mm) towards sense wires at a constant velocity of 9 μm/ns. Near the sense wires, they are accelerated by the fields and make avalanches of $\sim 10^5$ electrons which are detected by the sense wires. The xy position is calculated from the drift time under the assumption of constant drift velocity. The spatial resolution(in xy) for each wire is approximately 100 μm. The signal is read out at both ends to measure the z position by charge division. The measurement error of z position is approximately ± 1 mm in reconstruction of tracks. The momentum of the charged particle is determined by the hit information along the particle trajectory. In the barrel region, momentum resolution is formulated by

$$\frac{\sigma(p)}{p} = \sqrt{0.01^2 + (0.0025p)^2}. \tag{3.2}$$

Using the CCD hit constraint, momentum resolution is improved to

$$\frac{\sigma(p)}{p} = \sqrt{0.01^2 + (0.0015p)^2}. \tag{3.3}$$

The basic CDC parameters are summarized in Table 3.4.

3.2.3 Endcap Drift Chambers

At angles of less than 30° with respect to the beam axis, the tracking resolution and efficiency of the CDC degrades drastically since the tracks only pass through a fraction of CDC layers. The endcap drift chambers track charged particles in the forward and backward regions between 12° and 40°. The EDC consists of two sets of drift chambers, inner and outer, in both endcaps, placed at $z = \pm 1.2$ m and $= \pm 2.0$ m. Each of four drift chambers has three superlayers with a relative rotation 60°. The inner- and outer-chamber superlayers

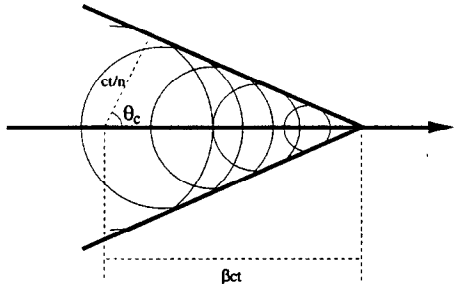

Figure 3.8: Cherenkov angle.

comprise 22 cells and 24 cells, respectively, with six sense wires per cell in both chambers. The maximum drift distance in a cell is 50 mm, and the average local resolution is $\sim 140\mu$ m. The momentum resolution[31] is $\sigma(p)/p = \sqrt{0.015^2 + (0.003p)^2}$.

3.2.4 Cherenkov Ring Imaging Detector

Particle identification in the SLD is performed by the Cherenkov Ring Imaging Detector(CRID). The CRID provides π, K and p separation over a wide range of momenta by measuring Cherenkov angles, not a simple yes/no decision between two particle species over a limited momentum range. The particle identification from the CRID with vertex information obtained by the VXD is expected to allows extremely clean charm and bottom signals to be obtained with high efficiency.

A charged particle at velocity above the speed of light in a medium emits Cherenkov photons coherently at a constant angle(θ_c) relative to the direction of motion(See Fig. 3.8). The speed of light in the medium is c/n where n is the index of refraction of the medium and c is the speed of light. The emission angle, θ_c, is given by the particle velocity, βc, and the speed of light in the medium:

$$\cos\theta_c = \frac{\frac{ct}{n}}{\beta ct} = \frac{1}{n\beta}, \tag{3.4}$$

where t is the time of flight of the particle.

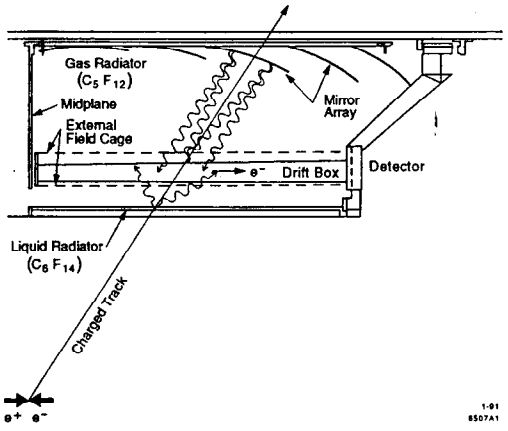

Figure 3.9: Schematic view of the barrel CRID.

A cross-section view of the barrel CRID is shown in Fig. 3.9. The barrel CRID consists of liquid radiators, drift boxes, gas radiators and mirrors. In Fig. 3.9, a charged particle passes through the CRID and produces Cherenkov lights in both liquid and gas radiator. The Cherenkov light emitted in the liquid radiator enters the drift box directly while the light produced in the gas radiator is focused back onto the drift box by spherical mirrors and forms a sharp image. The number of transmitted photons is 10~20 for both radiators. The drift box is filled with a gaseous mixture of C_2H_6 and 0.1% TMAE(Tetrakis Dimethyl Amino Ethylene). The photons from the both radiators pass through quartz windows on the front and back of the detector box and are converted to electrons by photo-ionization gaseous TMAE, which has a very high quantum efficiency in the wavelength range from 170 nm to 220 nm. The drift box is surrounded by a field cage, shown in Fig. 3.9, which provides a uniform electric field along z direction. The electrons are drifted by the electric field at constant velocity towards anode sense wires. Near the sense wires, they are accelerated, make avalanches of electrons before reaching anode. Three coordinates of the point of origin of photoelectron are measured as the drift time of the electron, the wire address and conversion

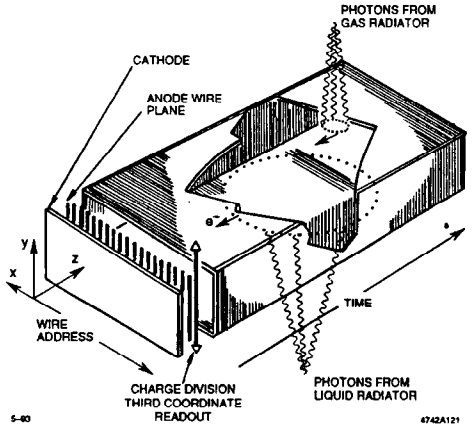

Figure 3.10: Schematic of the CRID drift box.

depth, which is determined by charge division(see Fig. 3.10). The basic parameters of the CRID are summarized in Table 3.5.

3.2.5 Liquid Argon Calorimeter

The measurement of energies of particles is done by the Liquid Argon Calorimeter(LAC). The LAC was designed to have excellent energy resolution both for electro-magnetic and hadronic particles and to be fully hermetic. For this purpose, the LAC was placed inside the magnet coil to avoid degrading the performance of the calorimeter due to energy absorption in the material of the coil. The LAC consists of barrel and endcap, each section has two electro-magnetic layers(EM1,EM2) and two hadronic layers(HAD1,HAD2). The shape of the barrel LAC is 6 m-long cylinder annulus with an inner radius of 2 m and an outer radius of 3 m.

The LAC is made of stacks of lead tiles interspersed by gaps filled with liquid argon(cell). Each cell is composed of a liquid argon ionization chamber, located between parallel lead electrodes, held apart by plastic spacers(Fig. 3.11, 3.12). The tiles are alter-

	Liquid	Gas
Radiator Material	C_6F_{14}	C_5F_{12}
Index of refraction	1.277	1.001725
Thickness of radiator	1 cm	$\sim$ 45 cm
Cherenkov angle ($\beta = 1$)	672 mrad	59 mrad
Radius of cherenkov ring ($\beta = 1$)	17 cm	2.9 cm
Number of photoelectrons ($\beta = 1$)	14	14
Momentum threshold		
e	1 MeV/c	9.5 MeV/c
π	0.23 GeV/c	2.6 GeV/c
K	0.80 GeV/c	9.1 GeV/c
p	1.50 GeV/c	17.3 GeV/c

Table 3.5: The barrel CRID parameters.

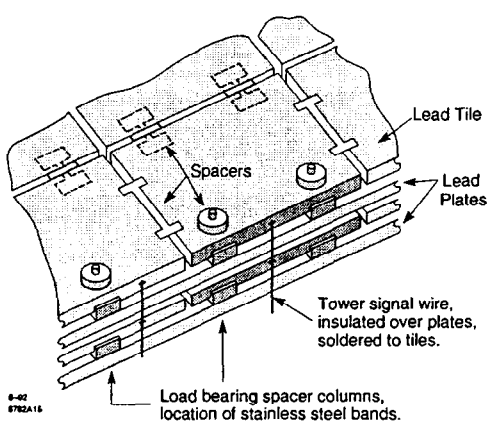

Figure 3.11: Schematic of LAC segment.

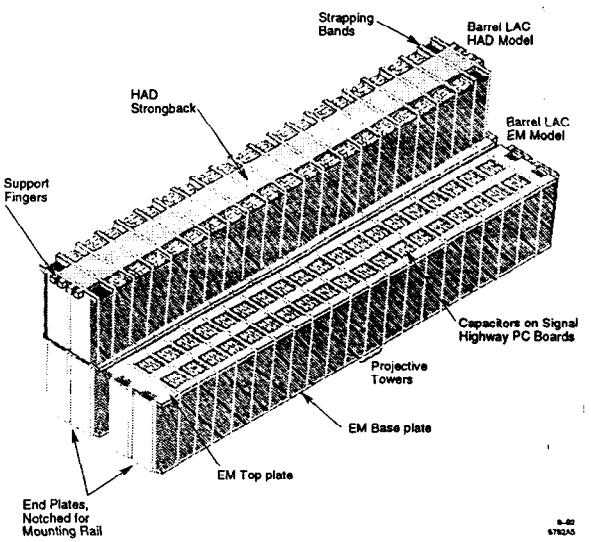

Figure 3.12: Schematic of LAC.

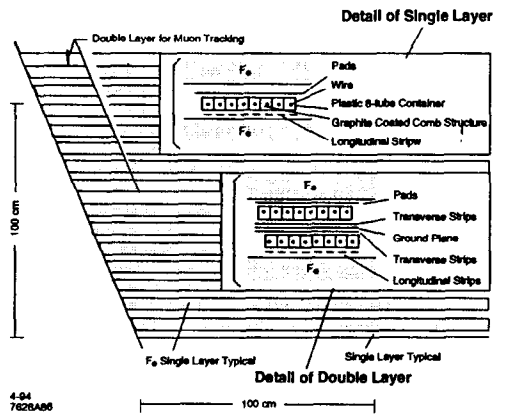

Figure 3.13: Schematic of the WIC layers.

nately at ground potential and at negative high voltage. Lead is used as absorber as well as electrodes. The LAC measures ionization in the liquid argon which is proportional to the energy loss of the incident particle. Therefore the energy of the particle is calculated from the collected charge. The resolution of energy measurement of the EM section is

$$\frac{\sigma(E)}{E} = \frac{0.08}{\sqrt{E}}. \tag{3.5}$$

That of HAD section is

$$\frac{\sigma(E)}{E} = \frac{0.55}{\sqrt{E}}. \tag{3.6}$$

3.2.6 Warm Iron Calorimeter

The Warm Iron Calorimeter(WIC) is the outer structure of the SLD, consisting of a barrel part and two endcap parts. The barrel part is divided into eight sections, which are 6.75 m long and 1.18 m thick. The WIC has three purposes : The first use is to absorb and measure the leakage of the hadronic showers from the LAC. The second is to identify muons. Finally,

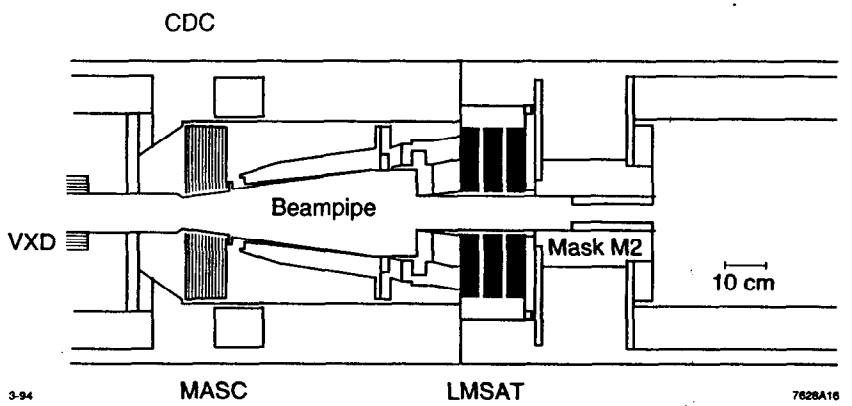

Figure 3.14: Schematic of the LUM.

the WIC serves as a flux return for the 0.6 T solenoidal magnetic field. The structure of the WIC is segmented into 14 layers, 50 mm thick iron with 32 mm gaps instrumented with streamer tubes as shown in Fig. 3.13. The tubes are made of the graphite coated plastic 9 mm × 9 mm tubes(1 mm thick) with 100 μm diameter Be-Cu wires. The tubes are filled with a gas mixture of 88% carbon dioxide, 9.5% isobutane and 2.5% argon and 4.75 kV high voltage is applied to the wires. On the top and bottom of the tubes, there are stripes of G10 plated with copper patterns in shapes of strips and pads. Charged particles create streamer discharges in the tubes, which induce signals on the strips and pads. The strips run parallel to the tubes to track muons. The pads are segmented so that they continue the projective tower geometry of the LAC to measure the shower energies. Fourteen layers of iron and streamer tubes are divided into two radial layers. The seventh and fourteenth layers are double layer chambers to give two-dimensional position information for muon tracking.

3.2.7 Luminosity Monitor

The Luminosity Monitor and Small Angle Tagger(LMSAT) and the Medium Angle Silicon Calorimeter(MASiC) measure electromagnetic showers in the 23-190 mrad region of θ. This measurement determines the integrated luminosity of the SLD by detecting Bhabha ($e^+e^- \to e^+e^-$) events. The cross section for this process, dominated by the photon exchange t-channel process, has been calculated with high precision. The LMSAT and MASiC are located on both sides of the IP. They are cones of silicon detector centered around the beampipe with a projective tower structure like the LAC. The LMSAT, a silicon-tungsten sampling calorimeter, covers the angles from 23 to 68 mrad at a distance of 1 m from the IP. It consists of 23 tungsten plates of 3.5 mm thickness, spaced 4.5 mm apart, for a total of 21 radiation lengths. Like the electromagnetic part of the LAC, the LMSAT is split up in EM1(first 6 layers) and EM2(remaining 17 layers). The MASC, lying at 31 cm from the IP and covering from 68 to 190 mrad, consists of ten 6.6 mm thick tungsten and is split up in EM1 and EM2. The energy resolution of the LMSAT is $23\%/\sqrt{E}$ and the angular resolution is $\delta\theta = 0.3$ mrad and $\delta\phi = 6.5$ mrad, which are adequate to measure Bhabha events.

3.2.8 Magnetic Coil

The magnet, located between the LAC and the WIC, is a 5.9 m diameter and 6.4 m long normal coil made of aluminum cooled by water. A magnetic field of 0.60 T in the center of the coil is provided by a current of 6600 A through 508 turns. The steel in the barrel and endcap WIC provides the return flux path for the magnetic field. The radial and z components of the magnetic field are given by

$$\begin{aligned} B_r &= B_r^0 \frac{rz}{r_0 z_0} \\ B_z &= B_z^0 + 0.5 B_r^0 \frac{r^2 - 2z^2}{r_0 z_0} \end{aligned} \tag{3.7}$$

where $B_r^0 = 0.0214$T, $B_z^0 = 0.601$T, $r_0 = 1.2$m and $z_0 = 1.5$m agrees with measured field to with 0.05% inside the CDC and to within 0.4% for the EDC. The uniformity of the field is more than adequate for the momentum measurements.

Parameter	Name	Default	Optimized value
Λ_{QCD}	PARE(21)	0.25 GeV	0.26 GeV
Q_0	PARE(22)	2.0 GeV	1.0 GeV
σ_q	PAR(12)	0.4 GeV	0.39 GeV
a	PAR(31)	0.50	0.18
b	PAR(32)	0.90 GeV^{-2}	0.34 GeV^{-2}

Table 3.6: Main parameters of JETSET 6.3.

3.3 SLD Monte Carlo

The Monte Carlo simulation has a very important role in this study, to determine the accurate detector efficiency and acceptance, and to estimate the performance of jet flavour tagging. The Z^0 hadronic decays are simulated by the JETSET 6.3[21] event generator with a hybrid heavy hadron decay model. The SLD detector response simulation is performed by using GEANT 3.15[32].

The parton shower option for the parton configuration and the string fragmentation option for the hadronization process are chosen for JETSET. Many parameters exist in JETSET to control the QCD and hadronization processes of the Z^0 decay products. We use the parameters determined by the TASSO collaboration[33], which have been found to be in good agreement with data at Z^0 resonance[34]. The major parameters used for the SLD simulation are listed in Table 3.6. The parameter Λ_{QCD} is the QCD scale parameter, described in chapter 2.4.2, used to determine parton branching. Q_0 is the cut-off mass of the parton shower evolution. σ_q is the width of the Gaussian transverse momentum distribution for the hadronization process in eq. 2.15. a and b are the parameters of the symmetric LUND fragmentation function in eq. 2.16.

For the heavy quark fragmentation function, the Peterson function[35] is chosen with $\epsilon_b = 0.006$ and $\epsilon_c = 0.06$ for b quark and c quark, respectively. The LEP experiments

Particles from B decay	$\langle N \rangle$ Monte Carlo	$\langle N \rangle$ Measurements
e	0.110	0.104 ± 0.004[8]
μ	0.110	0.103 ± 0.005[8]
τ	0.030	0.041 ± 0.010[8]
D^0	0.629	0.621 ± 0.026[42]
D^+	0.259	0.239 ± 0.037[42]
D_s	0.099	0.100 ± 0.025[42]
D^{*+}	0.236	0.230 ± 0.040[8]
Charmed baryon	0.060	0.064 ± 0.011[8]
J/ψ	0.014	0.013 ± 0.002[8]
$D^{(*)}D_s^{(*)}$	0.065	0.050 ± 0.009[8]
$\pi^{\pm}(direct)$	3.564	3.59 ± 0.11[43]
$K^{\pm}$	0.765	0.78 ± 0.04[43]
K^0	0.692	0.64 ± 0.04[43]
p	0.092	0.080 ± 0.005[8]
Λ	0.023	0.040 ± 0.005[8]

Table 3.7: Average numbers of particles from B_u and B_d mesons' decay.

have found that the M.C. simulation with those parameters reproduces the experimental data[36] well including the average total charged multiplicity of Z^0 hadronic events[37]. To be consistent with recent measurements of B meson decays, the M.C. parameters are tuned as follows[38]:

- Semileptonic decay

  The ISGW[39] form factor model is used for the semileptonic B meson decays. The branching fractions to e, μ and τ are set to 0.11, 0.11 and 0.03, respectively. D, D^* and D^{**} production fractions in the semileptonic decays are set to 0.33, 0.58 and 0.09, respectively. A total semileptonic decay branching fraction is 25%. The lepton momentum spectra from B_u and B_d with these parameters give good agreement with the recent CLEO data[40].

- Hadronic two body decay

  A total of 12.5% of the B meson branching fraction is set to the hadronic two body decays tabulated by the Particle Data Group[8].

- Baryon production

  A total of 6% is set to the charm baryon productions based on the CLEO measurement[41].

The remaining 56.5% of the branching fraction is attributed to the inclusive particle production fractions by using the modified JETSET heavy hadron decay package. Table 3.7 shows the comparison of the average number of particles produced by B_u and B_d decays between the data and the Monte Carlo simulation, and is indicating good agreement with data.

The detector simulation of the SLD is performed by GEANT 3.15, which provides the detector response to charged and neutral particles produced by the event generator. GEANT swims particles inside the SLD from the IP, according to particle momentum and the magnetic field with a geometric description of the SLD. During the swimming, multiple scattering, energy loss of the charged particle, nuclear interaction with the detector material,

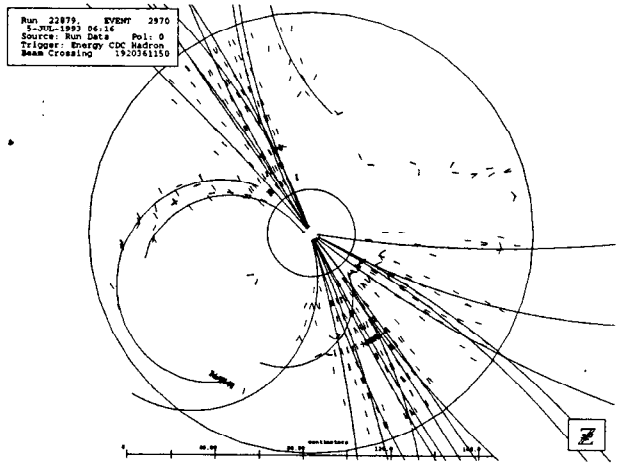

Figure 3.15: CDC vector hits with fitted tracks. Two vector hits per one cell are displayed. The circle in the center is the inner wall of the CDC. The tracks found in the CDC are extrapolated to the CDC and to the CRID.

delta ray and pair creation of photons are taken into account. Then the detector response is calculated with appropriate errors. To simulate the electronic readout noise and the beam backgrounds, the raw data produced by GEANT are overlaid with the experimental background data, taken by the random trigger as described in chapter 4.3. The random trigger data also provide information on the dead detector channels and the high voltage status of the CDC. Then, the overlaid raw data are processed by the same standard event reconstruction program as the real raw data are processed.

3.4 SLD Event Reconstruction

The event reconstruction of the SLD data is processed by the standard SLD event reconstruction package which is a collection of subsystem programs. The raw data are processed by each subsystem program first, and then all information is combined to a simple data struc-

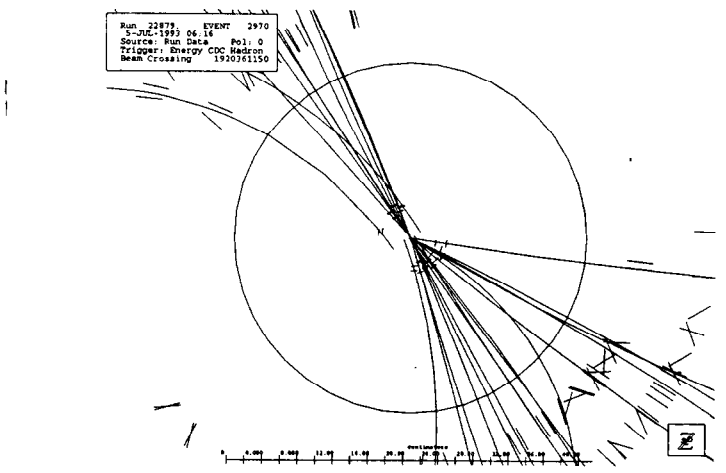

Figure 3.16: CDC hits linked to the CDC tracks. The circle is the CDC inner wall. Only the CCDs linked to the tracks are displayed. Tracks are extrapolated to the IP. Some vector hits in the CDC are also displayed.

ture. In the following, the reconstruction procedure for charged tracks is outlined, which are used in this analysis.

The main tracking device for charged particles is the CDC. The raw data of the CDC essentially contains hit information on sense wire number, charges measured at both ends of the sense wire and the time between the beam crossing and the arrival of the signal. The time information of the hit is converted to the drift distance using an appropriate drift velocity in the CDC cell. The drift velocity is a function of the gas pressure, gas temperature, gas mixture rate and electric filed in the cell. To obtain the drift velocity precisely, a drift speed monitor is installed in the CDC. After converting the drift time to the drift distance, we can calculate the ionization point, on which the charged particle passes, with information of the drift path calculated by the electric field in the CDC cell. Using all of the ionization points in the cell, two track segment vectors, called "vector hits", are determined by a fit which minimizes the χ^2 of residual distance of the ionization points to the track segment vector.

We have two vector hits because it is not possible to determine on which side electrons are drifted to the sense wires. This left-right ambiguity is solved by the pattern recognition with vector hits in superlayers. The CDC pattern recognition program[44] is also used to combine vector hits into the track(Fig. 3.15). Then, the track found in the CDC is tried to link to the CCD vertex detector hits to form a complete track(Fig. 3.16). Finally, the track is fitted to a helix trajectory, which gives the information of the charge and momentum of the charged particle associated with the track. The information of charge and momentum of the tracks is written to the Data Summary Tape(DST).

Chapter 4

Event Selection

In this chapter, we describe the Z^0 hadronic event selection procedure. The hadronic event selection is made in three stages. The first is an online event trigger. The second is an offline filter designed to select Z^0 hadronic and leptonic decay events. In the final stage, we select hadronic events in offline analysis.

We obtain $\sim 45,000$ hadronic events through those stages from the data collected by the SLD in 1992 and 1993 runs.

Before describing the hadronic event selection, we will review the properties of the data taking and summarize event topologies of Z^0 decays and physics background event.

4.1 Data Taking

In 1991, SLD data taking started with the engineering run. The electron beams were not polarized at that time. During three months, about 400 Z^0 decays were collected. The 1992 run began in June and ended in December with $\pm 22\%$ polarized electron beams. About 10,000 Z^0s were collected. In 1993, the run was started in March and ended in August. During those five months, about 50,000 Z^0 decays were collected with $\pm 63\%$ polarized electron beams. The electron polarization was improved by a newly-developed strained-lattice GaAs

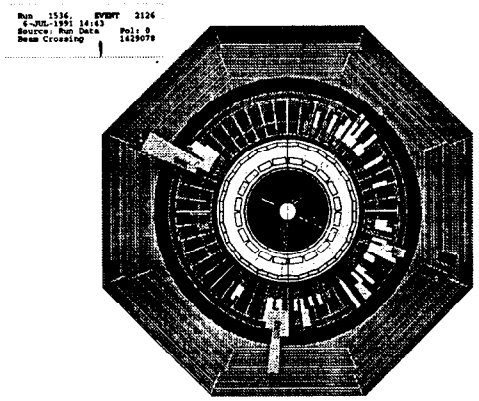

Figure 4.1: A hadronic event candidate with 4-jet event shape. From the center, CDC, CRID, LAC, Magnet and WIC are displayed. Charged tracks reconstructed by the CDC are, shown as white curves, extrapolated to outside of the CDC. Towers in the LAC and WIC represent amounts of energy deposits.

photocathode.

In this analysis, we use the data of 1992 and 1993. The data of 1991 was taken by different detector configuration and was not used for this analysis.

4.2 Event Topologies

The following are the event topologies considered for this study:

1. Z^0 hadronic decays($Z^0 \to f\bar{f} \to$ hadrons)

   70% of Z^0 decays are into hadrons. The charged multiplicity of a hadronic decay is large($\sim$ 20 average), and a large amount of energy is deposited in the calorimeters. The total momentum of the event is well balanced. A hadronic event candidate with 4-jet event shape is shown in Fig. 4.1.

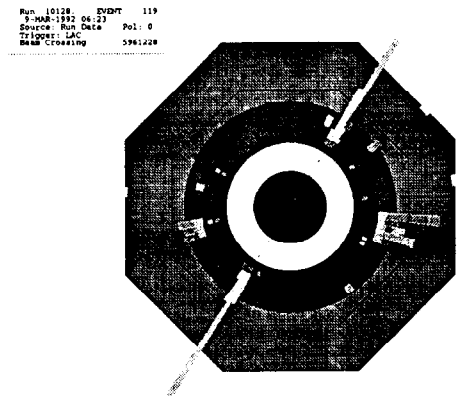

Figure 4.2: A wide angle Bhabha event candidate. Two back-to-back charged tracks, shown as white lines, are detected by the CDC(central black circle). They deposit all of their energies in the EM section of the LAC. Other energy deposits in the LAC are considered as beam related backgrounds.

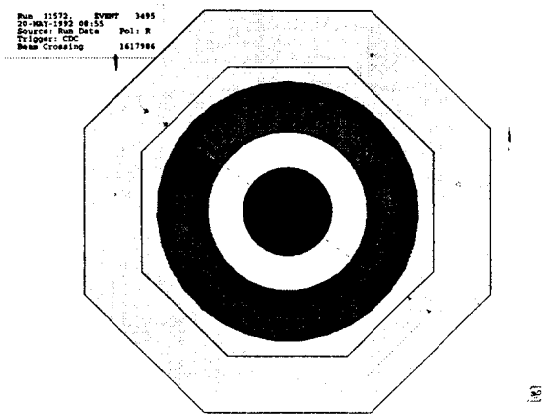

Figure 4.3: A μ pair event candidate. Two back-to-back charged tracks are detected by the CDC and the WIC. These tracks penetrate all calorimeters. There are small amounts of energy deposit in the LAC and WIC on their trajectories.

2. $Z^0 \to e^+e^-$, Bhabha events

   Bhabha events are detected by the LUM because they have small angle from beam axis. Bhabha electrons deposit all of their energy in just one or two electromagnetic calorimeter towers. The energies and momenta of the two tracks are balanced. A Bhabha event candidate is shown in Fig. 4.2.

3. $Z^0 \to \mu^+\mu^-$

   These events have two back-to-back tracks, like Bhabha events. Because most of those tracks penetrate all calorimeter layers, $\mu^+\mu^-$ events are easily identified. A μ pair event candidate is shown in Fig. 4.3.

4. $Z^0 \to \tau^+\tau^-$

   The τ decays into single charged track($\sim$85%) or three charged tracks($\sim$15%). Therefore about 25% of τ pair events have one track in a hemisphere and three tracks in the

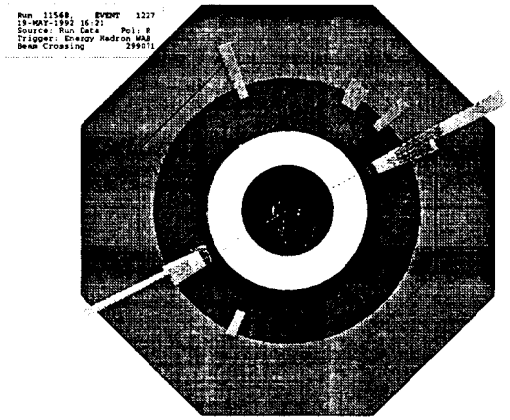

Figure 4.4: A τ pair event candidate. There are one track in right side and three tracks in left side.

other hemisphere. Their decay has at least one neutrino which is not detected by the SLD. So these events can be unbalanced in energy. A τ pair event candidate is shown in Fig. 4.4.

5. Two-photon processes

   The two-photon process is defined as $e^+e^- \to e^+e^-f\bar{f}$, where f is a quark or a lepton(Fig. 4.5 (a)). The e^+ and e^- in the final state travel along the beam axis and are not detected. If f is a quark, $f\bar{f}$ make two low energy hadron jets. The lepton pair or hadron jet pair are balanced in transverse momentum and are imbalanced in longitudinal momentum.

6. γ-γ process

   This is a pure QED process to exchange a virtual electron in t-channel. The Feynman diagram of this process is shown in Fig. 4.5 (b). The signature for the γ-γ process is two back-to-back 45 GeV photons.

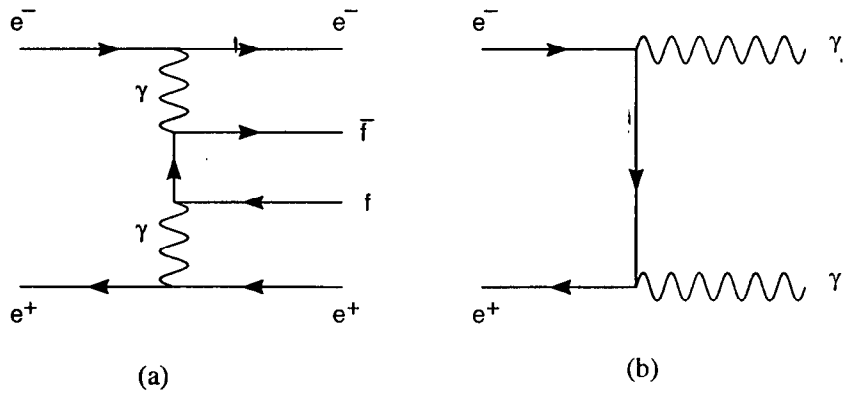

Figure 4.5: Feynman diagram of a two-photon process and a γ-γ process.

4.3 Event Trigger

The SLD trigger[45, 46] is designed to record Z^0 events efficiently, while vetoing beam related background as much as possible. In order to decide whether to accept or veto an event, either tracking devices(the CDC and the WIC) or calorimetry(the LUM and the LAC) are used. The trigger decision time is ~4 msec and typical readout time for the entire detector is about 200 msec. Typical trigger rates were 0.5 ~ 2 Hz, depending on the beam conditions. There are seven different triggers to record several kind of physics events on tape.

1. Energy

   The sum of energy deposits in the barrel and endcap LAC above thresholds is greater than 4 GeV, where the thresholds for the EM and HAD section are 154 MeV and 811 MeV, respectively. Only calorimetry information is read out by this trigger.

2. LUM

   The sum of energy deposits for each LUM EM2 section above threshold is greater than 12.5 GeV, where the threshold is 1.25 GeV. Calorimetry information is read out.

3. WAB

   The sum of energy deposits in the LAC EM section above threshold is 15 GeV, where threshold is 154 MeV. All subsystems are read out by this trigger.

4. Tracking

   Followings are required for this trigger:

   (a) at least two CDC tracks,

   (b) opening angle of two tracks > 30°,

   (c) trigger rate < 0.1 Hz.

   All subsystems are read out.

5. Hadronic

   There is at least one CDC tracks, and the energy trigger is satisfied. All subsystems are read out.

6. Muon

   There are two back-to-back barrel WIC tracks. All subsystems are read out.

7. Random

   This is triggered every 2,400 beam crossings(20 sec.). All subsystems are read out.

The energy thresholds shown above were changed several times. The actual readout thresholds for the data analysis are much lower(5/8/41/41 MeV for EM1/EM2/HAD1/HAD2). A CDC track is defined to have at least nine superlayer hits in the CDC, where the superlayer hit is defined to have at least 6 sense wire hits in a superlayer. A WIC track is defined to have at least 4 hits. The data taken by the Random trigger is used for background studies.

4.4 Offline Filter

This stage is needed to select good candidates of Z^0 hadronic decays and charged lepton pairs(e^+e^-,$\mu^+\mu^-$,$\tau^+\tau^-$) from the triggered events. To select hadronic decays, the following

criteria are required to be satisfied:

1. The total energy deposit in the barrel and endcap LAC is greater than 14 GeV.
2. The energy deposit in the endcap WIC < 11 GeV. This cut removes SLC muon backgrounds produced at up stream of the beams.
3. $E_{imb.} < 0.9$ and $(E_{imb.} + S) < 1$, where S is the sphericity[47] and $E_{imb.}$ is the energy imbalance defined as

$$E_{imb.} = \frac{E_{hem1} - E_{hem2}}{E_{hem1} + E_{hem2}}. \tag{4.1}$$

E_{hem1} and E_{hem2} are the energy deposits in the two hemispheres divided by the plane perpendicular to the sphericity axis. The sphericity S is defined by

$$S = \frac{3}{2} \min \left(\frac{\sum_i p_{iT}^2}{\sum_i p_i^2} \right) \tag{4.2}$$

where subscript T denotes transverse momentum to the axis, called sphericity axis, which minimizes the sum in the numerator. The sphericity lies in the range $0 \leq S \leq 1$. Events with $S \approx 1$ are rather spherical and events with $S \approx 0$ look like a back-to-back 2-jet.

To identify $\mu\bar{\mu}$, a pair of WIC strip tracks are required to be roughly back-to-back. A $\tau\bar{\tau}$ event is required to have at least one CDC good track with momentum greater than 1 GeV.

4.5 Hadronic Event Selection

The events passing the offline filter are fully reconstructed and written to data summary tapes. To select the events suitable for this analysis, we define good tracks first. Then good hadronic events are selected using the good tracks. The good tracks are selected by requiring

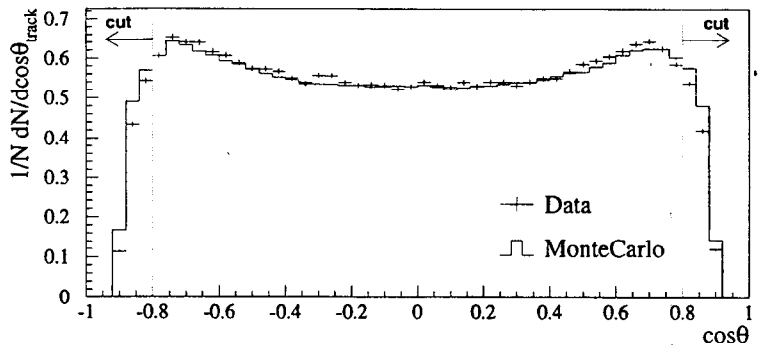

Figure 4.6: $\cos\theta$ distribution of charged tracks. Data and M.C. are normalized in the range $|\cos\theta_{track}| < 0.8$.

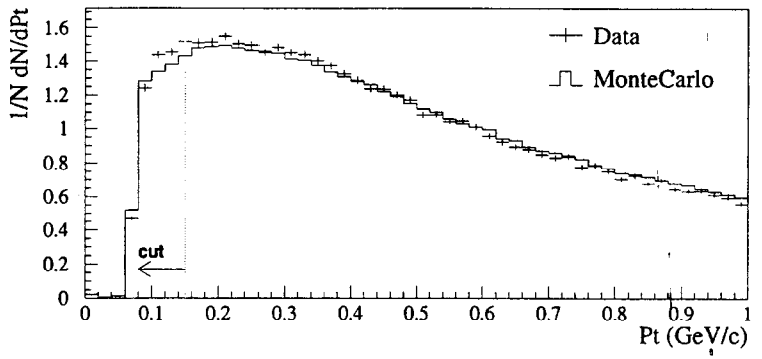

Figure 4.7: P_t distribution of charged tracks. Data and M.C. are normalized in the range $P_t > 0.15$.

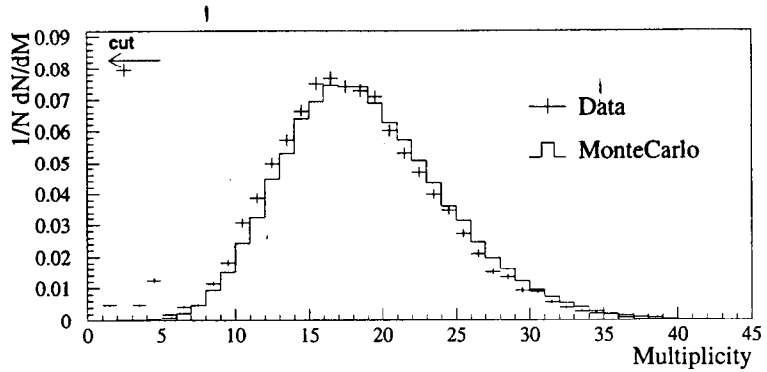

Figure 4.8: Charged multiplicity(n_{ch}) distribution of Z^0 hadronic decay candidates. Data and M.C. are normalized in the range $n_{ch} \geq 5$.

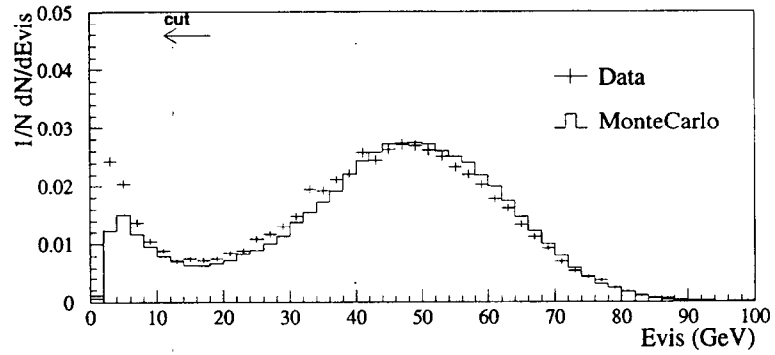

Figure 4.9: Visible energy(E_{vis}) distribution of Z^0 hadronic decay candidates. Data and M.C. are normalized in the range $E_{vis} > 0.2E_{cm}$.

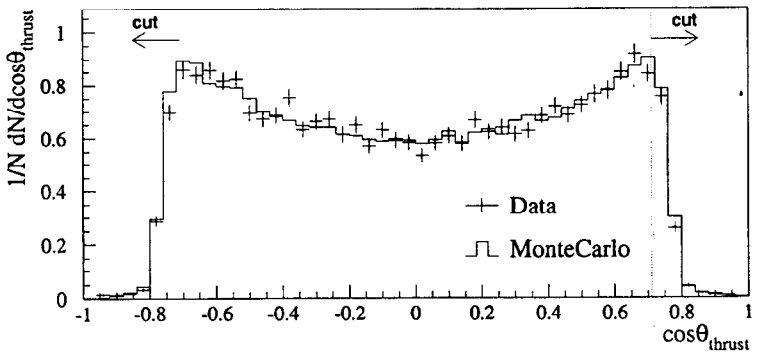

Figure 4.10: $\cos\theta_{thrust}$ distribution of Z^0 hadronic decay candidates. Data and M.C. are normalized in the range $|\cos\theta_{thrust}| < 0.7$.

1. $|\cos\theta_{track}| < 0.8$,
2. A transverse momentum(P_t) greater than 0.15 GeV/c,
3. $R < 5$ cm,
4. $|z| < 10$ cm.

Due to limited CDC coverage in polar angle, cut 1 is required. In Fig. 4.6, $\cos\theta_{track}$ distributions of the data and the M.C. are shown. In the central region, the M.C. reproduces the distribution of data well. Outside the coverage of the CDC($|\cos\theta| > 0.8$), the track reconstruction efficiency drops off, and the M.C. simulation slightly overestimates the tracking efficiency. Thus $\cos\theta = \pm 0.8$ is chosen to remove tracks which are poorly measured and are not simulated by the M.C. well. The P_t distributions of charged tracks is shown in Fig. 4.7. In the low P_t region, the M.C. simulation is different from the data which has slightly softer P_t spectrum. This is due to the difficulty of simulating multiple scattering of low momentum tracks. $P_t > 0.15$ GeV/c is chosen to ensure consistency between data and M.C. These low

momentum tracks are considered to be mostly originating from γ conversions. Cuts 3 and 4 using the track position closest to the IP, R and z, exclude the tracks which do not originate from the IP.

After the good track selection, the charged multiplicity(n_{ch}), the sum of charged track energy(called visible energy, E_{vis}) and the thrust axis[47] of the event is calculated with selected charged tracks. We apply following cuts to select hadronic events.

1. $n_{ch} \geq 5$,
2. $E_{vis} > 20\%$ of E_{cm}, where E_{vis} is the sum of energy of charged tracks assumed as pions,
3. $|\cos\theta_{thrust}| < 0.71$,
4. Maximum momentum of charged tracks in an event < 50 GeV/c.

In Fig. 4.8, the charged multiplicity distributions are shown. We observe an excess of low multiplicity events of the data for $n_{ch} < 5$. Those are expected to be lepton pairs and the beam related backgrounds which are not simulated in the M.C of hadronic events. Cut 1 is required to remove those lepton pairs and beam-related backgrounds. In Fig. 4.9, the E_{vis} distributions for the data and the M.C. are shown. We observe many low E_{vis} events in the data and these are not simulated in the M.C. Most of these events are considered to be beam related backgrounds. These backgrounds are eliminated by cut 2.

The thrust T, used in the cut 3, is defined as,

$$T = \max\left[\frac{\Sigma|\mathbf{p}_i \cdot \mathbf{t}|}{\Sigma|\mathbf{p}_i|}\right] \tag{4.3}$$

where i runs over all tracks, $\mathbf{p}_i$ is the momentum of track i and t is the thrust axis chosen to maximize the value of T. The distributions of $\cos\theta_{thrust}$ are shown in Fig. 4.10. Events with the thrust axis close to the beam direction($0.8 < |\cos\theta_{thrust}| < 1$) are not well reconstructed and not simulated well in the M.C. Thus those events are excluded in the analysis.

In Table 4.1, the track and event selections are summarized. The total number of selected hadronic events is 36,767 for both '92 and '93 runs.

Year	1992	1993
Before selection		
# of events after offline filter	39,673	107,268
# of tracks	270,573	1,033,781
Track selection		
# of good tracks	155,094	676,823
Event selection		
# of good tracks ≥ 5	9,304	41,865
$E_{vis}/E_{cm} > 0.2$	7,185	33,745
$\max(P) < 50$ GeV/c	7,098	33,436
$\|\cos\theta_{thrust}\| < 0.71$	6,446	30,321

Table 4.1: Summary of track selection and hadronic event selection. E_{vis} is the sum of energies of charged tracks. E_{cm} is the center of mass energy.

4.6 Background Estimation

The major sources of backgrounds in the hadronic events selected in previous section are $\tau^+\tau^-$ pairs, two photon processes and beam-related events. In this section, we estimate those background contaminations in our hadronic event samples. The total contamination of backgrounds in the hadronic event sample is estimated to be less than 0.4%. This value is considered to be negligible in this study because we apply more tight cuts for selecting good 3-jet events in this analysis. Thus, the background contaminations is not taken into account in further analysis.

4.6.1 $\tau^+\tau^-$ Events

The main τ decay mode is charged 1-prong decay[1] and its branching ratio is 85.5%[8]. The branching ratio into charged 3-prongs is 14.4%. Table 4.2 summarizes expected charged multiplicity of $\tau^+\tau^-$ events. In the hadronic event selection, we require at least 5 charged tracks in an event. This cuts out 97.7% of $\tau^+\tau^-$ events naively. A more precise estimation of $\tau^+\tau^-$ event contamination can be done using a Monte Carlo simulation. The same selection criteria as the hadronic Z^0 events are applied to a large number of generated M.C. $\tau^+\tau^-$ events. We have $4.20\% \pm 0.13\%$[48] of the $\tau^+\tau^-$ pairs which pass the cuts. This number is larger than the naive expected value 2.3% due to additional charged tracks in a $\tau^+\tau^-$ event created by radiative photon conversions or interactions in the detector material. The contamination of $\tau^+\tau^-$ pairs is estimated to be $0.20\% \pm 0.07\%$ by multiplying by the ratio $\mathrm{BR}(Z^0 \to \tau^+\tau^-)/\mathrm{BR}(Z^0 \to \mathrm{hadrons}) = 4.7$ %.

4.6.2 Two-Photon Processes

The cross section for this process is estimated to be 6.5 nb[49] at $\sqrt{s} = M_Z$, about one fifth of the hadronic cross section. However, these events are not energetic enough to trigger the detector. Most of events are very forward peaked and do not deposit a significant amount of

[1] one charged and multiple neutral particles

$\tau^+\tau^-$ decay mode	$\tau^+\tau^-$ decay charged multiplicity	Ratio
1-prong & 1-prong	2	73.1 %
1-prong & 3-prong	4	24.6 %
3-prong or more & 3-prong or more	6 or more	2.3 %

Table 4.2: Summary of $\tau^+\tau^-$ event multiplicity.

energy in the detector. As $\tau^+\tau^-$ background estimation, two photon processes are simulated by the M.C. It turns out that $0.5\% \pm 0.1\%$[48] of two photon processes pass the hadronic event selection cuts. The rate of two photon processes in hadronic event sample is therefore estimated to be $0.10\% \pm 0.03\%$.

4.6.3 Beam Related Events

The events caused by the interactions of the beam with the beam pipe wall or a nucleon of a residual gas atom inside the beam pipe are called beam-related events. It is very hard to calculate the cross sections for these events because they strongly depend on the beam conditions which can vary over a short period of time. The contamination of these events was estimated to be less than 0.1%[48].

Chapter 5

Analysis

In this chapter, we make three samples of quark and gluon jets by jet flavour tagging and compare them. First of all, using the Durham jet finding algorithm, we find 3-jet events containing two quark jets(q and $\bar{q}$) and one gluon jet. Then, we make three statistically independent samples called the "gluon tagged" sample, the "light mixture" sample, and the "heavy mixture" sample by jet flavour tagging of light quarks(u,d,s) and heavy quarks(c,b). The gluon tagged sample is enriched with gluon jets. The light(heavy) mixture is the mixture sample containing light(heavy) quark jets and gluon jets. These three samples have different compositions of flavour and thus allow us to compare properties of quark and gluon jets. In particular, we compare three jet properties:charged multiplicity, inclusive energy fraction and angular width. To unfold the pure state of light quark, heavy quark and gluon jet, we use the M.C. to estimate the compositions of each jet sample. Only charged tracks are used in this analysis.

5.1 Three Jet Event Selection

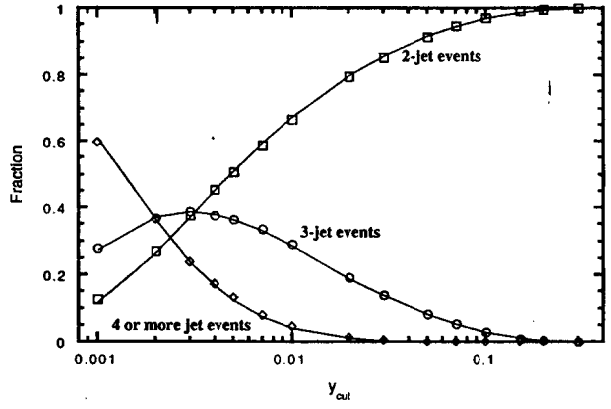

Figure 5.1: n-jet rates as a function of y_{cut} with Durham jet finder. The symbols represent the data points; □:2-jet events, ○:3-jet events, ◇:4 or more jet events. The solid curves represent the M.C.

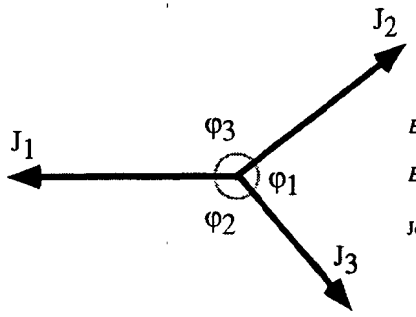

E_i^{vis} : Sum of visible energy in jet number i

$$E_i^{jet} = E_{CM} \frac{\sin\varphi_i}{\sin\varphi_1 + \sin\varphi_2 + \sin\varphi_3}$$

Jets are ordered by jet energies : $E_1^{jet} > E_2^{jet} > E_3^{jet}$

Figure 5.2: Definition of variables for 3-jet event. Three arrows represent jet axes.

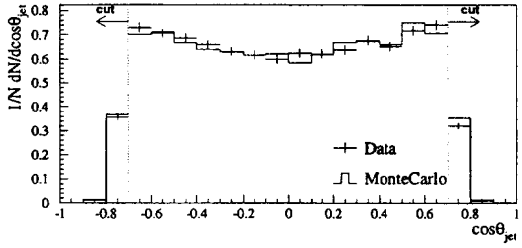

Figure 5.3: $\cos\theta_{jet}$ distribution of jets in 3-jet events.

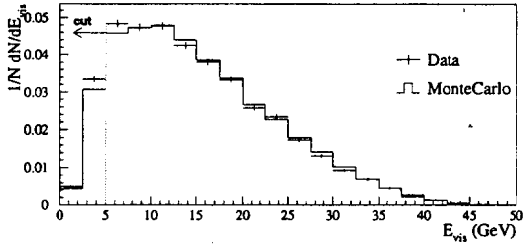

Figure 5.4: E_{vis} distribution of jets in 3-jet events.

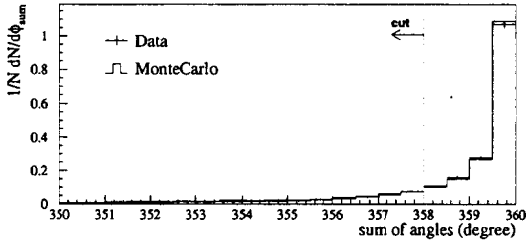

Figure 5.5: $\sum\phi_i$ distribution of jets in 3-jet events.

In order to select 3-jet events, we apply the $k_\perp$(Durham) jet finder[50] to the selected hadronic events. In each hadronic event, the quantity

$$y_{ij} \equiv \frac{2\min(E_i^2, E_j^2)(1-\cos\theta_{ij})}{E_{vis}^2}, \tag{5.1}$$

is calculated for all pairs of particles i and j, where E_i and E_j are the energies of two particles, θ_{ij} is the opening angle between them, and E_{vis} is the sum of the energies of all particles in the event. We assume that all charged particles are pions in this analysis. Two particles(or jets) i and j with the smallest y_{ij} in the event are combined as a jet if y_{ij} is smaller than a certain threshold value y_{cut}. The four-momentum of the combined jet is equal to the vector sum of the constituent particles. This procedure is repeated until all y_{ij} exceed y_{cut}. Fig. 5.1 shows the n-jet rates as a function of y_{cut} from data(symbols) and M.C. simulation(solid lines). The number of found jets depends on y_{cut}. At $y_{cut} = 0.003$, the fraction of 3-jet events is maximized. However, the fractions of 2-jet and 4 or more jet events change very much around $y_{cut} = 0.003$. Therefore, the 3-jet event sample found around 0.003 includes 2-jet or 4-jet like events which will be removed after the "well measured 3-jet event selection", described later. To obtain the maximized fraction of "well measured 3-jet event", we choose y_{cut} value 0.007.

After selecting 3-jet events using the Durham jet-finder, we apply further cuts to obtain well-measured events. Fig. 5.2 shows a schematic of a 3-jet event. The three arrows represent the axes of the jets determined by the jet-finder. E_i^{vis} is the sum of particle energies contained in a jet. φ_i is the angle opposite to the jet i. The jets are ordered by jet energy($E_{jet,i}$) as $E_{jet,1} > E_{jet,2} > E_{jet,3}$. $E_{jet,i}$ is calculated in terms of E_{CM} and the angles φ_i(Fig. 5.2) by

$$E_{jet,i} \equiv E_{CM}\frac{\sin\varphi_i}{\sin\varphi_1 + \sin\varphi_2 + \sin\varphi_3}. \tag{5.2}$$

The following cuts are applied to obtain well-measured 3-jet events.

1. $|\cos\theta_{jet}| < 0.7$,

   where θ_{jet} is the polar angle of a jet. This is required for all 3 jets so that all jets are contained in the sensitive barrel region of the CDC. In Fig. 5.3, the distributions of

   $\cos\theta_{jet}$ are shown for the data and the M.C., representing that the jet reconstruction efficiency drops at $\cos\theta_{jet} > 0.7$ and $\cos\theta_{jet} < -0.7$.

2. $E^{vis} > 5.0$ GeV,

   In Fig. 5.4, the E_{vis} distributions are shown for the data and the M.C. A jet with low visible energy is considered to be a low energy jet or a jet with large missing energy. The error on the jet axis determination increases as E_{vis} gets smaller. Thus we require that E_{vis} of all jets in an event is greater than 5 GeV.

3. $\sum_i \varphi_i > 358°$,

   $\sum_i \varphi_i$ is the sum of the angles between jets, and should be 360° if we measure all particles in an event perfectly because the Z^0 decays at rest. The deviation of the sum of the angles from 360° in Fig. 5.5 is due to the effect of undetected neutral particles and measurement error of charged track momenta. We exclude poorly measured events which lie in the long tail in Fig. 5.5.

Fig. 5.6 shows a display of a typical 3-jet event which satisfies the 3-jet event selection criteria. Table 5.1 summarizes the 3-jet events from the data and the M.C. obtained from this selection. We obtain 5,693 good 3-jet events out of 36,767 hadronic events, corresponding to 15.4% of the hadronic events.

5.2 Flavour Tagging of Jets

Flavour tagging of jets is based on the long lifetime of heavy quarks(b and c) and their large boost in Z^0 decays due to the hard fragmentation functions. The average momentum of B mesons produced by the Z^0 decay is $\sim$ 38 GeV/c and its average decay length is $\sim$ 2.2 mm. Therefore, tracks from the heavy hadron decay typically have large impact parameters[51] and large transverse momenta relative to the initial hadron direction due to the large mass of the heavy hadron. The impact parameter(b) is defined as the closest approach of the extrapolated track to the IP in the x-y plane, as shown in Fig. 5.7. The IP used to measure

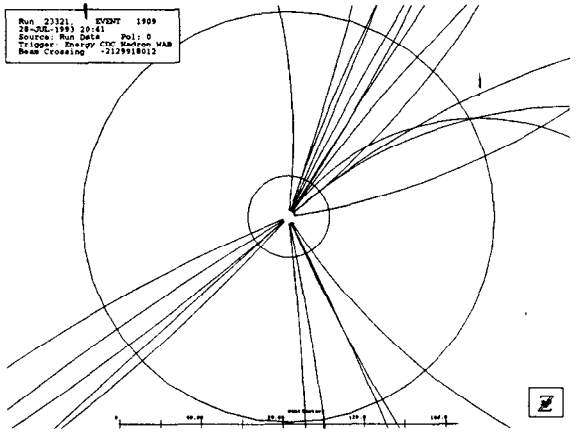

Figure 5.6: A hadronic event candidate with three jets. The charged particles tracked by the CDC are shown as curves. The inner and outer wall of the CDC are also shown. The tracks are extrapolated to the CDC vertex detector.

Cuts	Data		Monte Carlo	
	# of events	Ratio to 3-jet events	# of events	Ratio to 3-jet events
3-jet events	11,729	1.0	46,864	1.0
$\lvert\cos\theta_{jet}\rvert < 0.7$	9,428	0.804 ± 0.011	37,384	0.798
$E^{vis} > 5.0$ GeV	7,216	0.615 ± 0.009	29,660	0.633
$\sum_i \varphi_i > 358$	5,693	0.485 ± 0.008	23,872	0.509

Table 5.1: Summary of 3-jet event selection.

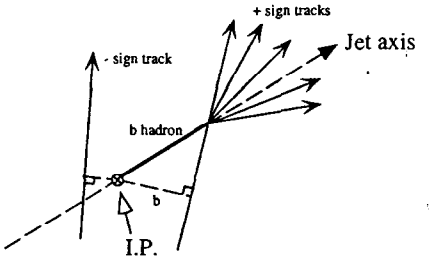

Figure 5.7: Definition of the impact parameter.

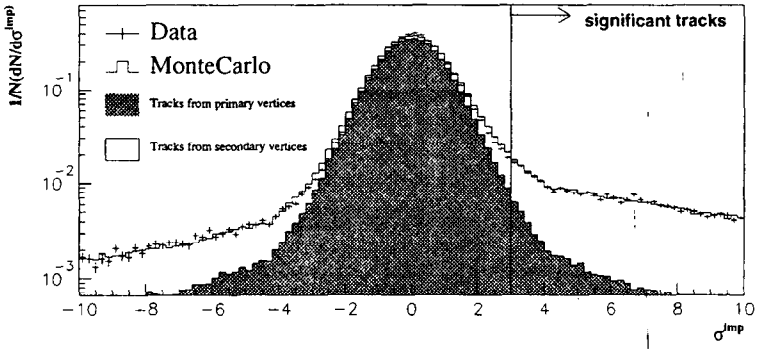

Figure 5.8: Weighted impact parameter(σ^{imp}) distribution. The tracks with $\sigma^{imp} > 3$ are defined as the significant tracks, which is used for the jet flavour tagging.

the impact parameter is determined by fits to events close in time to the event under study[1]. Heavy quark jet tagging is made by a precise measurement of the impact parameter and independent determination of the IP position for each event.

The weighted impact parameter(σ^{imp}) is defined as

$$\sigma^{imp} \equiv \frac{b}{\delta b} \tag{5.3}$$

where b is the impact parameter and δb is its measurement error. The sign of the impact parameter is determined by the position of the crossing point of the jet axis and the track(Fig. 5.7). If the crossing point is in front(back) of the IP, *plus*(*minus*) sign is assigned.

The distribution of the weighted impact parameter of the data is shown as crosses in Fig. 5.8. The histogram shows the M.C. simulation, in which the contributions of the tracks originated from the IP(primary vertex; shaded) and originated from the secondary vertices(non-shaded) are shown separately. The M.C. simulation reproduces the distribution of the data well. The distribution is seen to be asymmetric with more entries at positive values of the weighted impact parameter than at negative values. The M.C. shows that such an asymmetry is caused by the tracks from secondary vertices. On the other hand, the tracks from the IP have a normal distribution with mean value zero. Such asymmetry enables us to tag jet flavour as heavy or light quark. We define a *significant track* to have a weighted impact parameter greater than a certain value, $\sigma^{imp}_{sig.}$, with high tracking quality. The following criteria are required to select the significant tracks:

1. $\sigma^{imp} > \sigma^{imp}_{sig.}$,
   where $\sigma^{imp}_{sig.} = 3$ in this analysis,
2. radius of track starting point < 40 cm,
3. more than 40 hits in the CDC,
4. $|z|$ at the closest approach to the IP < 1.5 cm,

[1]The SLC beam size is very small and stable in the transverse dimensions[51]. Its size was $2.2 \otimes 2.2$ μm^2 in 1992 and was reduced to $2.4 \otimes 0.8$ μm^2 in 1993.

5. CDC track fit quality $\chi^2/df < 5$,
   where df is the number of degree of freedom in the CDC track fit,
6. at least one good VXD hit,
7. CDC and VXD combined fit quality $\chi^2/df < 10$,
   where df is the degree of freedom in the CCD and CDC combined fit,
8. impact parameter $b < 3$ mm,
9. the error of impact parameter $\delta b < 250\mu$m.

We assume that such significant tracks originate from the secondary vertices of heavy hadrons. The significant tracks are used to tag heavy- and light-quark jets. Heavy-quark jets are tagged by requiring two or more significant tracks in a jet. Light-quark jets are tagged by no significant tracks in a jet.

Using this jet flavour tagging method, we classify the following three samples of jets.

(a) Gluon Tagged sample:

We first assume that the highest energy jet in a 3-jet event is a quark jet[2]. In the 3-jet configuration, it is most probable to be a quark(or anti-quark) jet because of the bremsstrahlung nature of gluon radiation from the initial quarks. The probability that the highest energy jet is a quark jet is estimated to be 93.5% by the M.C. Thus, the two lower energy jets are quark and gluon jets. If one of two lower energy jets is tagged as a heavy quark jet, then we can anti-tag the remaining jet as a gluon jet. We refer to the anti-tagged gluon jets hereafter as "gluon tagged"(Fig. 5.9 (a)). Fig. 5.10 shows an event display around the IP, which has a gluon tagged jet.

(b) Light Mixture sample:

The jet flavour tagging method is applied to the highest energy jet in an event. If this jet is tagged as a light quark jet, then the remaining two lower energy jets are taken

[2]See Appendix D

Sample	Number of jets	Compositions		
		Gluon	Light Quark	Heavy Quark
Gluon tagged	739	86.5 %	4.5 %	9.0 %
Light mixture	8,096	49.7 %	38.7 %	11.6 %
Heavy mixture	1,654	51.7 %	2.8 %	45.5 %

Table 5.2: Summary of three jet samples.

to be a "light mixture" sample, which include quark and gluon jets(Fig. 5.9 (b)). In this sample, light quark jets are enriched. In this selection procedure, it is probable that there are some events which have a jet also tagged as a gluon jet. Such events are removed from this sample.

(c) Heavy Mixture sample:

This sample is the same as the light mixture sample, however the highest energy jet is tagged as a heavy quark jet. In this sample, heavy quark jets are enriched(Fig. 5.9 (c)).

These three samples are statistically independent of each other. It is known that the heavy flavour tagging efficiency is high for the high multiplicity jets and is relatively low for the low multiplicity jets because we count the significant tracks in the flavour tagging. To remove such a tagging bias, the jets which are used for the jet flavour tagging are not included in the above samples. This is automatically required in the above selection procedure.

The numbers of jets in each sample are listed in Table 5.2 and are shown in Fig. 5.11 as a function of jet energy. The compositions of flavours for the three samples, obtained from the M.C., are also shown in Fig. 5.11. In the gluon tagged sample, we have a peak around 15 GeV due to the phase space of gluon emission from a quark. The contamination of quark jets in the gluon tagged sample is only 13.5 % in total.

(a) Gluon Tagged Sample

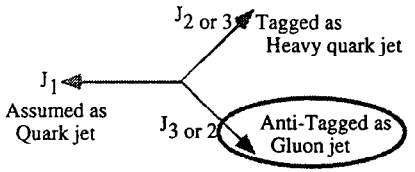

(b) Light Mixture Sample

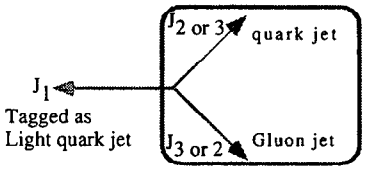

(c) Heavy Mixture Sample

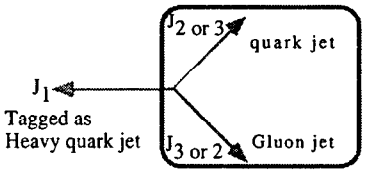

Figure 5.9: Three samples of tagged jets.

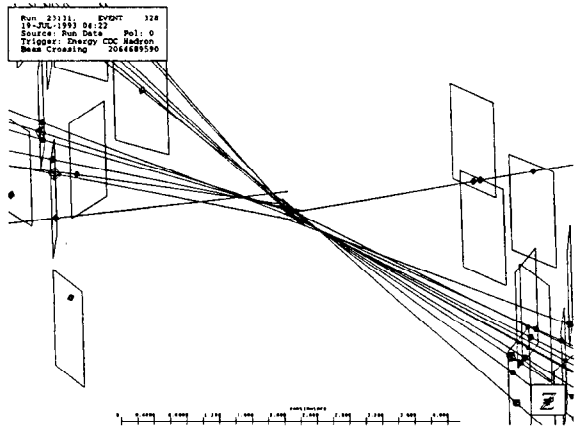

Figure 5.10: A 3-jet event with a gluon tagged jet. Charged tracks, shown as lines, are extrapolated into the IP, the center of this display. Polygons represent the CCD vertex detector with hits. Hit points are shown as diamond symbols. Two displaced vertices are formed in the right side and the lower left wide jets. These jets are tagged as a heavy quark jet. The remaining jet, upper left side, is anti-tagged as a gluon jet.

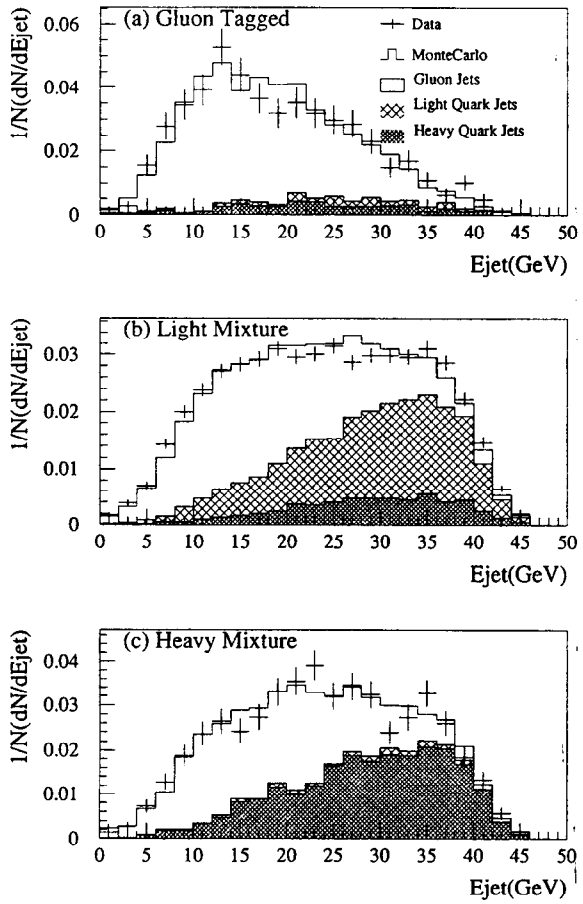

Figure 5.11: E_{jet} distribution of three samples.

5.3 Comparison of Jet Properties for Raw Samples

We choose three fundamental jet properties to compare quark and gluon jets: charged multiplicity, inclusive energy fraction and jet width. In the following we make comparisons of these properties between the three jet samples.

5.3.1 Charged Multiplicity

Charged multiplicity is a simple count of charged tracks assigned to a jet by the Durham jet finder. In Fig. 5.12, the average charged multiplicities, $\langle n_{ch} \rangle$, of the three samples are shown as a function of jet energy(E_{jet}). The error bars shown in Fig. 5.12 represent statistical errors only. As the jet energy gets larger, the errors on the gluon tagged sample increase, while the errors on the two other samples decrease. This is due to the statistics of the samples as shown in Fig. 5.11. The gluon tagged and the heavy mixture have almost the same $\langle n_{ch} \rangle$ in all energy regions. In all energy regions, the average charged multiplicities of the gluon tagged sample have a tendency to be larger than those of the light mixture sample. At $E_{jet} = 36$ GeV, the charged multiplicity ratio of the gluon tagged to the light mixture is 1.21 ± 0.06, which exceeds unity by 3.5 standard deviations. Thus it is indicated that gluon jets yield a larger multiplicity than light quarks in this energy region. $\langle n_{ch} \rangle$ of all samples drop at last bin($E_{jet} = 41$ GeV). This can be considered that most of those jets are from 2-jet like events and the reconstruction of jets is imperfect. Therefore, we exclude those marginal jets from further analysis. We also exclude first bin($0 < E_{jet} \leq 8$ GeV) for the same reason. In Table 5.3, the average jet energy $\langle E^{jet} \rangle$, average visible energy, and $\langle n_{ch} \rangle$ for three samples are listed.

5.3.2 Inclusive Energy Fraction

Inclusive energy fraction X_E is defined as

$$X_E \equiv \frac{E_{particle}}{E_{jet}^{vis}}, \tag{5.4}$$

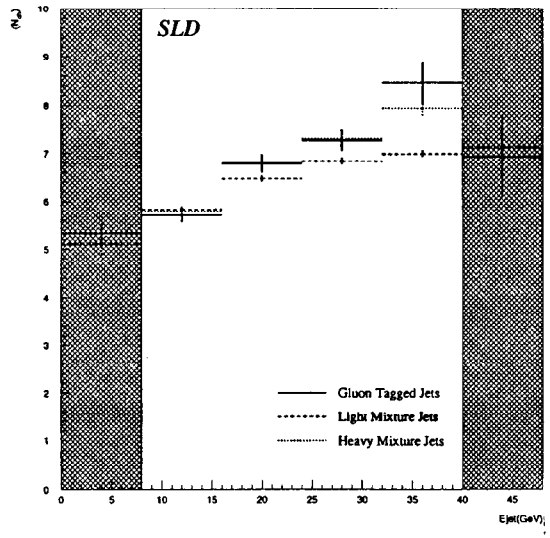

Figure 5.12: Average charged multiplicities.

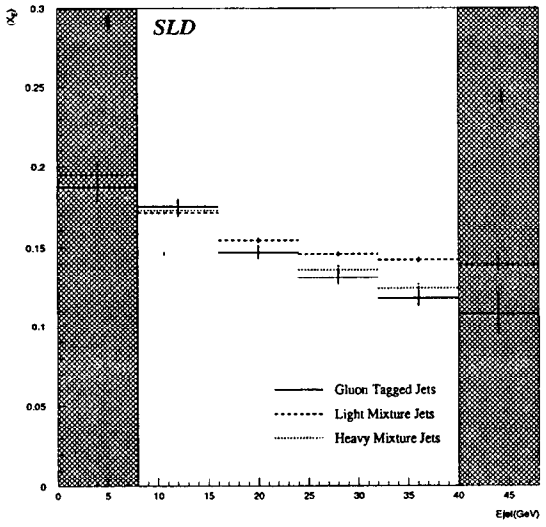

Figure 5.13: Inclusive energy fraction(X_E).

where $E_{particle}$ is the energy of charged particle assumed as a pion and E_{jet}^{vis} is the visible energy of a jet to which the charged particle is assigned. In Fig. 5.13, the average inclusive energy fractions, $\langle X_E \rangle$, are shown as a function of jet energy. In this plot, the particles between the axes of two lower energy jets are removed. This is due to an overlap of the jets and an ambiguity of track assignment to the jet. In Fig. 5.13, the gluon tagged sample has a softer energy fraction compared to the light mixture. This is consistent with the results of $\langle n_{ch} \rangle$, since we compare $\langle X_E \rangle$ at the same jet energy. In Table 5.3, $\langle X_E \rangle$ for the three samples are listed.

5.3.3 Jet Width

In this analysis, the jet width is defined as the average angle, θ, between the particle momentum vector and the jet axis. In Fig. 5.14, the average jet width, $\langle \theta \rangle$, is shown as a function

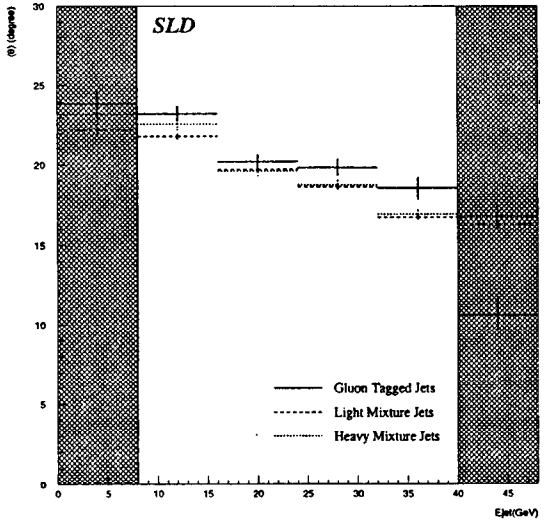

Figure 5.14: Average jet width.

of jet energy, indicating the jet width decreases with the jet energy. The distributions for the light mixture and the heavy mixture are the same within statistical errors. However, the gluon tagged sample has larger $\langle \theta \rangle$ in all energy regions except in the last bin. We exclude tracks between two lower energy jets for the same reason as the inclusive energy fraction. In Table 5.3, $\langle \theta \rangle$ for the three samples is listed.

5.4 Unfolding Distributions for Pure States

The measured distributions, shown in the previous section, are the results of mixed samples of light quark, heavy quark and gluon states with three different fractions. Furthermore, they are affected by the finite detector resolution, acceptance, and efficiency. To obtain the distributions for pure states of light quark, heavy quark and gluon jets, we unfold the distributions presented in the previous section, and correct for the detector effects.

Bin	Sample	$\langle E_{jet} \rangle$	$\langle E^{vis} \rangle$	$\langle n_{ch} \rangle$	$\langle X_E \rangle$	$\langle \theta \rangle$
1	Gluon Tagged	6.02 ± 0.19	7.36 ± 0.26	5.32 ± 0.21	0.187 ± 0.009	23.87 ± 0.86
	Light Mixture	5.59 ± 0.09	7.74 ± 0.14	5.12 ± 0.10	0.195 ± 0.004	22.21 ± 0.35
	Heavy Mixture	5.52 ± 0.22	8.24 ± 0.51	5.09 ± 0.18	0.194 ± 0.008	23.23 ± 0.85
2	Gluon Tagged	12.34 ± 0.14	8.73 ± 0.17	5.71 ± 0.15	0.175 ± 0.004	23.25 ± 0.46
	Light Mixture	12.29 ± 0.06	9.41 ± 0.09	5.84 ± 0.06	0.171 ± 0.002	21.79 ± 0.18
	Heavy Mixture	12.20 ± 0.13	9.03 ± 0.18	5.79 ± 0.13	0.173 ± 0.004	22.63 ± 0.42
3	Gluon Tagged	19.95 ± 0.17	11.55 ± 0.27	6.79 ± 0.19	0.147 ± 0.004	20.20 ± 0.44
	Light Mixture	19.98 ± 0.05	12.63 ± 0.10	6.47 ± 0.06	0.154 ± 0.001	19.74 ± 0.15
	Heavy Mixture	20.26 ± 0.11	12.68 ± 0.20	6.78 ± 0.12	0.147 ± 0.003	19.61 ± 0.31
4	Gluon Tagged	27.41 ± 0.18	14.97 ± 0.44	7.27 ± 0.22	0.131 ± 0.004	19.83 ± 0.51
	Light Mixture	27.98 ± 0.05	15.90 ± 0.13	6.82 ± 0.06	0.146 ± 0.001	18.59 ± 0.15
	Heavy Mixture	27.78 ± 0.11	15.81 ± 0.27	7.31 ± 0.15	0.136 ± 0.003	18.72 ± 0.31
5	Gluon Tagged	35.23 ± 0.31	18.25 ± 0.89	8.46 ± 0.42	0.118 ± 0.005	18.52 ± 0.70
	Light Mixture	35.74 ± 0.05	19.40 ± 0.18	6.99 ± 0.06	0.142 ± 0.001	16.73 ± 0.15
	Heavy Mixture	35.71 ± 0.12	18.75 ± 0.37	7.95 ± 0.17	0.124 ± 0.003	16.91 ± 0.31
6	Gluon Tagged	41.58 ± 0.44	16.19 ± 2.30	6.93 ± 0.84	0.108 ± 0.013	10.64 ± 1.03
	Light Mixture	41.73 ± 0.07	20.66 ± 0.45	7.14 ± 0.16	0.139 ± 0.003	16.31 ± 0.32
	Heavy Mixture	41.75 ± 0.17	16.56 ± 0.78	7.12 ± 0.34	0.140 ± 0.007	16.78 ± 0.64

Table 5.3: Jet properties of three samples.

The relation between the measured and the pure states may be written

$$\begin{pmatrix} M_{gluon\,tag.}(e_i) \\ M_{light\,mix.}(e_i) \\ M_{heavy\,mix.}(e_i) \end{pmatrix} = U_i \begin{pmatrix} G(e_i) \\ L(e_i) \\ H(e_i) \end{pmatrix}, \tag{5.5}$$

where $M_{gluon\,tag.}(e_i)$, $M_{light\,mix.}(e_i)$, and $M_{heavy\,mix.}(e_i)$ represent the measured quantities for a given jet energy bin e_i. $G(e_i)$, $L(e_i)$ and $H(e_i)$ are the values for the pure states of gluon, light quark and heavy quark jets, respectively. U_i, "unfolding matrix", is the 3×3 matrix for bin i, and contains all information on flavour compositions and detector effects for the three measured samples. Therefore, U_i can be written in terms of a "composition matrix", C_i, and a "detector effect matrix", D_i,

$$U_i = C_i \cdot D_i. \tag{5.6}$$

The composition matrix is explicitly written

$$C_i = \begin{pmatrix} c_{gluon}^{gluon\,tag.} & c_{light\,quark}^{gluon\,tag.} & c_{heavy\,quark}^{gluon\,tag.} \\ c_{gluon}^{light\,mix.} & c_{light\,quark}^{light\,mix.} & c_{heavy\,quark}^{light\,mix.} \\ c_{gluon}^{heavy\,mix.} & c_{light\,quark}^{heavy\,mix.} & c_{heavy\,quark}^{heavy\,mix.} \end{pmatrix}, \tag{5.7}$$

where $c_{gluon}^{gluon\,tag.}$ is the fraction of true gluon jets in the gluon tagged sample, and so on. The detector effect matrix is a diagonal matrix

$$D_i = \begin{pmatrix} d_{11} & 0 & 0 \\ 0 & d_{22} & 0 \\ 0 & 0 & d_{33} \end{pmatrix}. \tag{5.8}$$

The pure states of gluon, light quark, and heavy quark can be obtained by inverting eq. 5.5

$$\begin{pmatrix} G(e_i) \\ L(e_i) \\ H(e_i) \end{pmatrix} = U_i^{-1} \begin{pmatrix} M_{gluon\,tag.}(e_i) \\ M_{light\,mix.}(e_i) \\ M_{heavy\,mix.}(e_i) \end{pmatrix}$$

$$= D_i^{-1} \cdot C_i^{-1} \begin{pmatrix} M_{gluon\,tag.}(e_i) \\ M_{light\,mix.}(e_i) \\ M_{heavy\,mix.}(e_i) \end{pmatrix}, \quad (5.9)$$

To obtain the composition matrices and the detector effect matrices, two sets of M.C. are used: the hadron level Monte Carlo and the detector level Monte Carlo:

1. Hadron level Monte Carlo

   200,000 events are generated by the JETSET 6.3 without any detector simulation. Only charged particles with generated momenta are used for the analysis. Jets are determined by the Durham jet finder with y_{cut} value 0.007, as the same value as used in the data analysis. Their flavour are tagged using generator information.

2. Detector level Monte Carlo

   This is the M.C. described in chapter 3.3. About 360,000 events are generated by the JETSET 6.3, and are processed by the SLD simulation program. The output data of M.C., which is the same format as the data, is analyzed by exactly the same procedure as the real data.

The composition matrices are determined by the detector level M.C. which has information on generated jet flavour and flavour tagged by the analysis. The composition matrices for each jet energy bin are listed in Table 5.4. From the table, the gluon jet fraction in the gluon tagged sample amounts to a high value of 93.5% at the jet energy $8 \sim 16$ GeV. However, the gluon jet fraction in both the light and the heavy mixtures are also high. This is the reason why we do not expect to observe significant differences in the distributions presented in previous section. At high energy($32 \sim 40$ GeV) region, the gluon, light, and heavy quark fractions are dominant in the gluon tagged, light, and heavy mixture samples, respectively. We observe differences among the three samples at the high energy.

The diagonal elements of the detector effect matrices are obtained by the bin-by-bin

correction method using the above two sets of M.C.

$$d_{11} = \frac{G(e_i)}{M'_{gluon}(e_i)},$$
$$d_{22} = \frac{L(e_i)}{M'_{light\,quark}(e_i)},$$
$$d_{33} = \frac{H(e_i)}{M'_{heavy\,quark}(e_i)}, \quad (5.10)$$

where $M'_{gluon}(e_i)$, $M'_{light\,quark}(e_i)$ and $M'_{heavy\,quark}(e_i)$ are calculated by

$$\begin{pmatrix} M'_{gluon}(e_i) \\ M'_{light\,quark}(e_i) \\ M'_{heavy\,quark}(e_i) \end{pmatrix} = C_i^{-1} \begin{pmatrix} M_{gluon\,tag.}(e_i) \\ M_{light\,mix.}(e_i) \\ M_{heavy\,mix.}(e_i) \end{pmatrix}. \quad (5.11)$$

In Table 5.4, the diagonal elements of the correction matrix are listed. At the high energy, the correction factors deviate from unity largely.

5.5 Comparison for Pure State Samples

5.5.1 Average Charged Multiplicity

In Fig. 5.15(a), the unfolded $\langle n_{ch} \rangle$ and their statistical errors for gluon, light quark and heavy quark jets are shown as a function of jet energy. While the statistical errors in the lower energy bins are larger than the differences between gluon and quark jets, it is obvious that gluon jets have the largest value in all energies and light quark jets have the smallest value in most energy regions except the lowest energy bin.

A function $\langle n_{ch} \rangle = a \ln(E_{jet}) + b$ is used to fit those distributions. The fitted curves are also shown in Fig. 5.15 for these distributions. Fitted values of a, b and reduced χ^2 are listed in Table 5.5. $\langle n_{ch} \rangle$ of heavy quark jets is well described by the function with reduced χ^2 0.2. Except for the last bin, gluon jets also well described by the function. The fitted function of light quark jets is almost flat due to a drop of the last bin which has a small error.

Jet energy bin(GeV)	Composition matrices	Correction matrices $\langle n_{ch} \rangle$	Correction matrices $\langle X_E \rangle$	Correction matrices $\langle \theta \rangle$
	$\begin{pmatrix} c^{\text{gluon tag.}}_{\text{gluon}} & c^{\text{gluon tag.}}_{\text{light quark}} & c^{\text{gluon tag.}}_{\text{heavy quark}} \\ c^{\text{light mix.}}_{\text{gluon}} & c^{\text{light mix.}}_{\text{light quark}} & c^{\text{light mix.}}_{\text{heavy quark}} \\ c^{\text{heavy mix.}}_{\text{gluon}} & c^{\text{heavy mix.}}_{\text{light quark}} & c^{\text{heavy mix.}}_{\text{heavy quark}} \end{pmatrix}$	$\begin{pmatrix} d_{11} \\ d_{22} \\ d_{33} \end{pmatrix}$	$\begin{pmatrix} d_{11} \\ d_{22} \\ d_{33} \end{pmatrix}$	$\begin{pmatrix} d_{11} \\ d_{22} \\ d_{33} \end{pmatrix}$
$8 \sim 16$	$\begin{pmatrix} 0.935 & 0.017 & 0.048 \\ 0.776 & 0.180 & 0.044 \\ 0.792 & 0.018 & 0.190 \end{pmatrix}$	$\begin{pmatrix} 0.98 \\ 1.18 \\ 1.20 \end{pmatrix}$	$\begin{pmatrix} 1.02 \\ 0.75 \\ 0.80 \end{pmatrix}$	$\begin{pmatrix} 0.90 \\ 0.91 \\ 0.89 \end{pmatrix}$
$16 \sim 24$	$\begin{pmatrix} 0.880 & 0.034 & 0.086 \\ 0.609 & 0.297 & 0.094 \\ 0.648 & 0.020 & 0.332 \end{pmatrix}$	$\begin{pmatrix} 1.00 \\ 1.02 \\ 0.98 \end{pmatrix}$	$\begin{pmatrix} 1.03 \\ 0.97 \\ 0.94 \end{pmatrix}$	$\begin{pmatrix} 0.93 \\ 0.92 \\ 0.83 \end{pmatrix}$
$24 \sim 32$	$\begin{pmatrix} 0.805 & 0.090 & 0.105 \\ 0.406 & 0.451 & 0.143 \\ 0.416 & 0.030 & 0.554 \end{pmatrix}$	$\begin{pmatrix} 1.00 \\ 0.95 \\ 1.06 \end{pmatrix}$	$\begin{pmatrix} 1.06 \\ 0.93 \\ 0.90 \end{pmatrix}$	$\begin{pmatrix} 0.98 \\ 0.76 \\ 0.85 \end{pmatrix}$
$32 \sim 40$	$\begin{pmatrix} 0.659 & 0.148 & 0.193 \\ 0.220 & 0.608 & 0.172 \\ 0.238 & 0.043 & 0.719 \end{pmatrix}$	$\begin{pmatrix} 0.88 \\ 1.05 \\ 1.10 \end{pmatrix}$	$\begin{pmatrix} 1.22 \\ 0.71 \\ 0.89 \end{pmatrix}$	$\begin{pmatrix} 1.06 \\ 0.63 \\ 0.89 \end{pmatrix}$

Table 5.4: Summary of the composition and the correction matrices. Only the diagonal elements are listed for the correction matrices. The off-diagonal elements of the correction matrices are zero.

Jet flavour	a	b	reduced χ^2
Gluon jet	2.6 ± 0.5	-0.7 ± 1.3	2.7
Light quark jet	0.2 ± 0.6	5.1 ± 2.1	0.7
Heavy quark jet	1.5 ± 0.9	1.7 ± 3.0	0.2

Table 5.5: Fitted values and reduced χ^2.

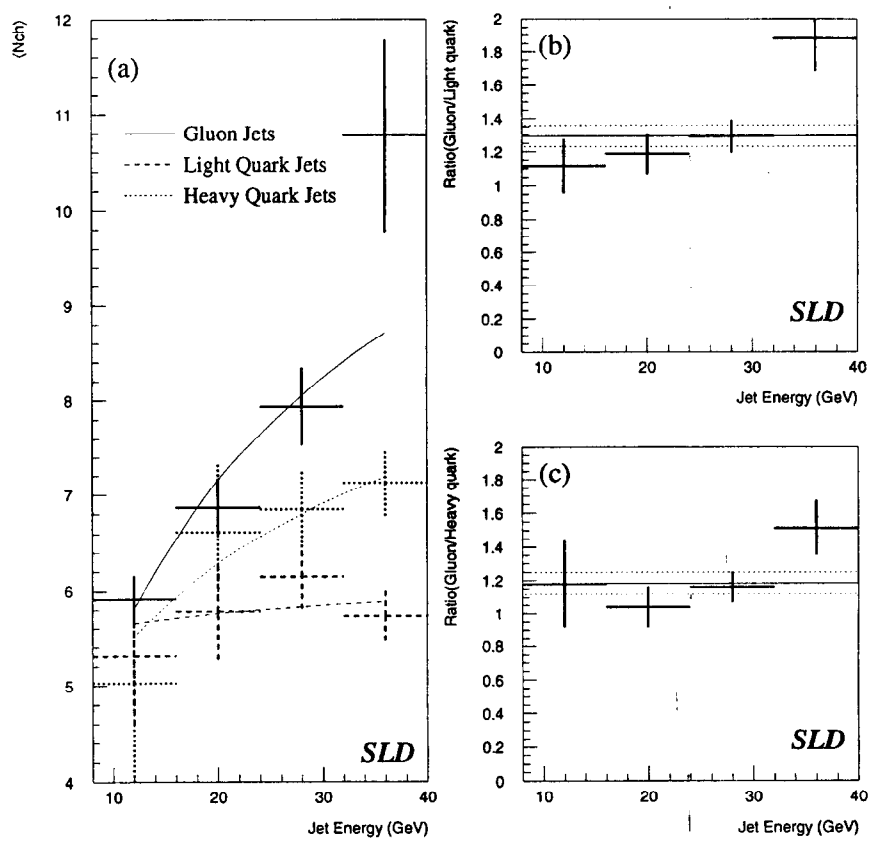

Figure 5.15: Average charged multiplicities $\langle n_{ch} \rangle$ and their ratios.

	ratio	statistical error	systematic error
$\langle n_{ch} \rangle$			
gluon to light quark	1.294	± 0.064	$^{+0.047}_{-0.064}$
gluon to heavy quark	1.183	± 0.063	$^{+0.068}_{-0.035}$
$\langle X_E \rangle$			
gluon to light quark	0.707	± 0.033	$^{+0.073}_{-0.077}$
gluon to heavy quark	0.793	± 0.043	$^{+0.061}_{-0.077}$
$\langle \theta \rangle$			
gluon to light quark	1.120	± 0.048	$^{+0.040}_{-0.024}$
gluon to heavy quark	1.172	± 0.055	-0.056

Table 5.6: The final ratios of gluon to quark jets.

In Fig. 5.15(b) and (c), the ratios of gluon to light quark, and gluon to heavy quark jets are shown respectively. The solid lines in these plots are weighted averages over all four bins and the dotted lines indicate $\pm 1\sigma$ errors. The ratios seem to increase with the jet energy. However, the errors on the ratios are not small enough to conclude the energy dependence of the ratios from our result. The weighted average ratio of gluon to light quark jets is 1.29 ± 0.06 for $E_{jet} = 8 \sim 40$ GeV. This is a 4.8 standard deviation excess from unity. The data point in the last bin shows an exceptional value but its error is large. So the effect of the last bin on the fitting is small. The ratio of gluon to heavy quark jets is 1.18 ± 0.06. Again, the data point in last bin scatter from the average ratio with a large error. However, the weighted average of the charged multiplicity ratio of gluon to heavy quark jets is larger than unity by three standard deviations. These results indicate that gluon jets have a larger charged multiplicity than light quark and heavy quark jets. The ratios are summarized in Table 5.6 with statistical and systematic errors. In the next section(chapter 5.6), the systematic errors will be discussed.

5.5.2 Average Inclusive Energy Fraction

The corrected distributions of $\langle X_E \rangle$ and their ratios are shown in Fig. 5.16, in the same manner as $\langle n_{ch} \rangle$ plots. These plots should be correlated with the corresponding plots of $\langle n_{ch} \rangle$ because $\langle n_{ch} \rangle \cdot \langle X_E \rangle = E_{jet}^{vis}$ and E_{jet}^{vis} are almost the same for the three jets. Certainly, we can see such correlations between $\langle n_{ch} \rangle$ and $\langle X_E \rangle$. Gluon jets have smaller energy fraction and light quark jets have larger energy fraction, as contrasted with $\langle n_{ch} \rangle$. The weighted average ratios of gluon to light quark and gluon to heavy quark jets are 0.70 ± 0.03 and 0.79 ± 0.04, respectively. These values are less than unity by 10 standard deviations and 5.3 standard deviations, respectively. These values and their errors are displayed in the ratio plots as a solid line and dotted lines respectively. From these results, we can conclude that gluon jets have softer energy spectrum than quark jets. The ratios decrease as jet energy increases within the energy region shown in the plots. The ratios are summarized in Table 5.6.

5.5.3 Average Jet Width

Fig. 5.17(a) shows the corrected distributions of $\langle \theta \rangle$ and their ratios. In Fig. 5.17, $\langle \theta \rangle$ of light and heavy quarks are roughly flat, while that of gluon jets decrease with the jet energy. In the energy region shown in the plot, we observe that gluon jets are wider than quark jets. Since the differences of $\langle \theta \rangle$ among jets decrease with the jet energy, $\langle \theta \rangle$ is not a good observable for the comparison of jet widths in the higher energy regions. In Fig. 5.17(b) and (c), the ratios of gluon to light quark and gluon to heavy quark jets are shown, respectively. In both plots, the ratios are roughly flat except for the lowest energy bin. The weighted ratio of $\langle \theta \rangle$ for gluon to light quark is 1.12 ± 0.05, and that of gluon to heavy quark is 1.17 ± 0.06. Thus we conclude that the jet width of gluon jets are wider than quark jets within the present region of jet energy. The ratios are summarized in Table 5.6.

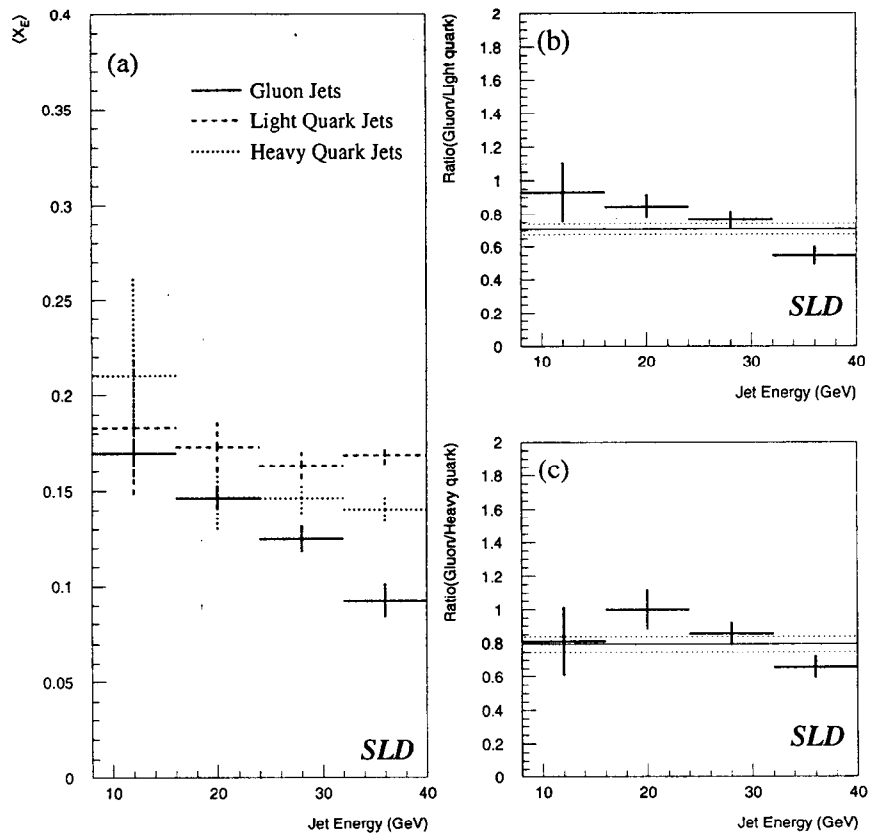

Figure 5.16: Average inclusive energy fractions $\langle X_E \rangle$ and their ratios.

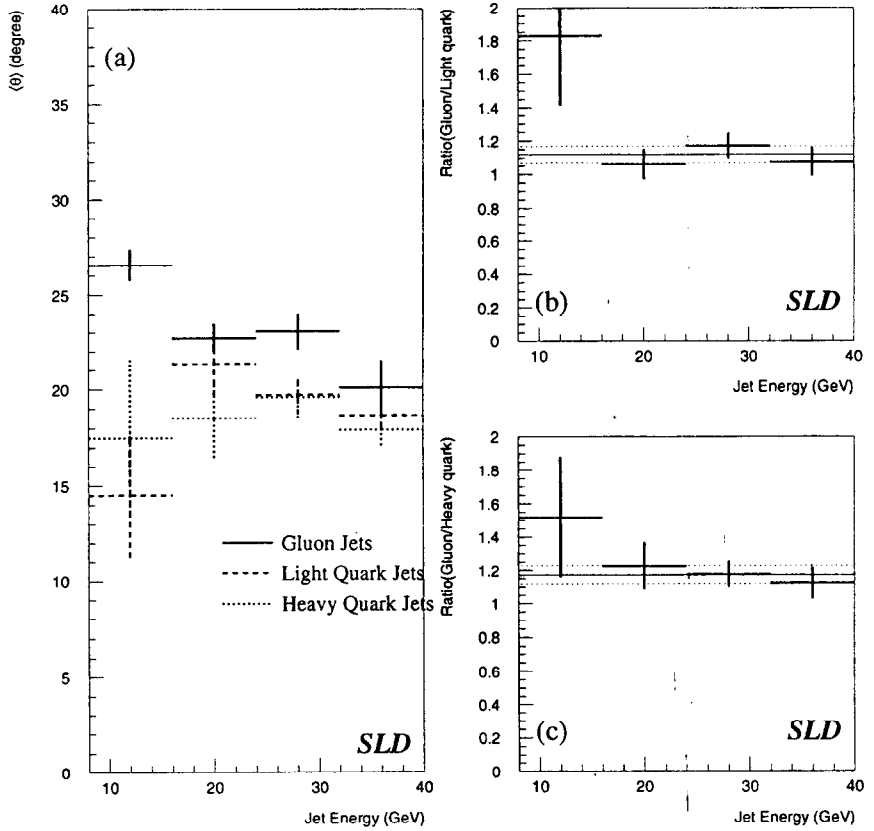

Figure 5.17: Average jet widths $\langle \theta \rangle$ and their ratios.

5.6 Systematic Errors

In this section, we discuss the systematic errors for the ratios given in the previous section. The systematical error is the uncertainty other than the statistical error, and comes from, for instance, the selection criteria applied for the data. In general, if a M.C. simulation describes the data perfectly, the biases introduced from the event selection would be exactly corrected by using the M.C. simulation, and we would have no systematic error due to the selection. However, we have no information how exactly the M.C. simulation describes our data. Consequently, we need to examine the systematic errors introduced from several selection criteria used in the analysis.

To examine the systematic errors, we consider the following five possible sources:

1. track and event selection,
2. detector modeling,
3. 3-jet event selection,
4. jet tagging, and
5. Monte Carlo modeling.

To estimate the systematic error from the track and event selection, we shift the $|\cos\theta|$ cut criteria by 0.1 from the standard cut, for instance, and calculate the differences of the ratios for $\langle n_{ch}\rangle$, $\langle X_E\rangle$ and $\langle\theta\rangle$ between the standard and the shifted cuts. The shift value of 0.1 is chosen somewhat arbitrarily. However, we choose the shift within the possible maximum shift considering the reproducibility of the M.C. simulation to the data. Similarly, we calculate the differences for the rest of the cuts. In Appendix B, the detailed estimates of the systematic errors are described. The total shift from the standard selection is calculated by adding each of the differences in quadrature. In Table 5.7, the systematic errors coming from each source are listed. $\Delta R^{G/L}_{syst.}$ and $\Delta R^{G/H}_{syst.}$ represent the systematic errors of the ratio of gluon to light quark jets and that of gluon to heavy quark jets, respectively. The amounts of the systematic errors are the same level as those of the statistical errors.

Categories	$\langle n_{ch}\rangle$	$\langle X_E\rangle$	$\langle\theta\rangle$
	$\Delta R^{G/L}_{syst.}$	$\Delta R^{G/L}_{syst.}$	$\Delta R^{G/L}_{syst.}$
	$\Delta R^{G/H}_{syst.}$	$\Delta R^{G/H}_{syst.}$	$\Delta R^{G/H}_{syst.}$
Track and event selection	± 0.047	± 0.072	± 0.024
	± 0.035	± 0.060	~ 0
Detector modeling	~ 0	~ 0	$+0.032$
	$+0.027$	~ 0	~ 0
3-jet event selection	~ 0	-0.029	~ 0
	$+0.051$	-0.049	-0.032
Jet tagging	-0.043	$+0.015$	~ 0
	~ 0	$+0.009$	-0.046
Monte Carlo model	~ 0	~ 0	~ 0
	~ 0	~ 0	~ 0
Total	$^{+0.047}_{-0.064}$	$^{+0.073}_{-0.077}$	$^{+0.040}_{-0.024}$
	$^{+0.068}_{-0.035}$	$^{+0.061}_{-0.077}$	-0.056

Table 5.7: Summary of systematic errors. $\Delta R^{G/L}_{syst.}$ and $\Delta R^{G/H}_{syst.}$ represent the systematic errors of the ratio of gluon to light quark jets and that of gluon to heavy quark jets, respectively.

Chapter 6

Summary

In this thesis, we have studied quark and gluon jet differences in 3-jet events of Z^0 hadronic decays with charged tracks. The use of weighted impact parameters allows us to identify the flavour of jets, as light or heavy quark jets. Gluon jets are collected by anti-tagging of heavy quark jets with a purity of 86.6% estimated from the Monte Carlo simulation. For comparison, we considered the light mixture and the heavy mixture of quark and gluon jets. The light and the heavy mixture samples consist of two lower energy jets of 3-jet events in which the highest jet is tagged as a light quark jet or a heavy quark jet, respectively. These three samples are statistically independent. The jets used for jet flavour tagging are not included in the three samples so that the bias introduced by the jet flavour tagging was minimized.

Three observables are chosen to compare the jet properties:the charged multiplicity $\langle n_{ch} \rangle$, the inclusive energy fraction of particles $\langle X_E \rangle$, and the average angle between the particle momentum and the jet axis $\langle \theta \rangle$, called the jet width. By the use of the M.C. simulation, the distributions of jet properties obtained from the three samples are unfolded to obtain the properties for pure states of gluon, light quark, and heavy quark jets. The observables for pure states include corrections for the detector resolution and acceptance.

Our results show that $\langle n_{ch} \rangle$ of gluon jets are larger than those of light quark and heavy quark jets in the jet energy region of 8 GeV to 40 GeV. The ratios of $\langle n_{ch} \rangle$ increases with

the jet energy. However, the errors of ratios are not small so that we can not conclude the jet energy dependence of the ratios from our result. The ratios of $\langle n_{ch} \rangle$ are measured to be

$$R_{ch} = 1.294 \pm 0.064(\text{stat.})^{+0.047}_{-0.064}(\text{syst.})$$
$$R_{ch} = 1.183 \pm 0.063(\text{stat.})^{+0.068}_{-0.035}(\text{syst.})$$

for gluon to light quark and gluon to heavy quark, respectively. The statistical errors take into account the correlations between the numerator and denominator, and the systematic errors are estimated by varying the criteria for the track, hadronic event and 3-jet event selection, the parameters of jet flavour tagging, the parameters of heavy quark(b and c quark) Monte Carlo models. Fig. 6.1 shows the comparison of our results with recent measurements[1]. All results in Fig. 6.1, except for the QCD calculation, are measured using Z^0 hadronic decay 3-jet events, as described in Chapter 2.3. The symbols, R_{ch} and R, represent the multiplicity ratio of charged particles and both charged and neutral particles, respectively. To compare the results from the LEP experiment, we calculate $R_{ch}(gluon/quark)$ from the results of $R_{ch}(gluon/light\,quark)$ and $R_{ch}(gluon/heavy\,quark)$ using the ratios of $\text{Br}(Z^0 \to light\,quarks)$ and $\text{Br}(Z^0 \to heavy\,quarks)$. We note that the results in Fig. 6.1 are measured with the different range of jet energies. However, our results are averaged in the jet energy range($8 < E_{jet} < 40$) so that the averaged jet energy is 24 GeV. This average energy is the same as for the OPAL results in which they used the symmetric 3-jet events for the analysis. Fig. 6.1 indicates that R_{ch} of our result and the LEP measurements are in good agreement within their errors. The size of our measurement error is comparable to that of the OPAL measurement even with lower statistical data than the OPAL experiment. This is because our analysis method is different and the gluon jet tagging efficiency is higher. All experimental results are systematically lower than the ratio from the Monte Carlo based QCD prediction of 1.38, however $R_{ch}(gluon/light\,quark)$ of our results is consistent with the

[1]The total error is a quadratic sum of the statistical error and the systematic error. No systematic errors are estimated in the DELPHI results.

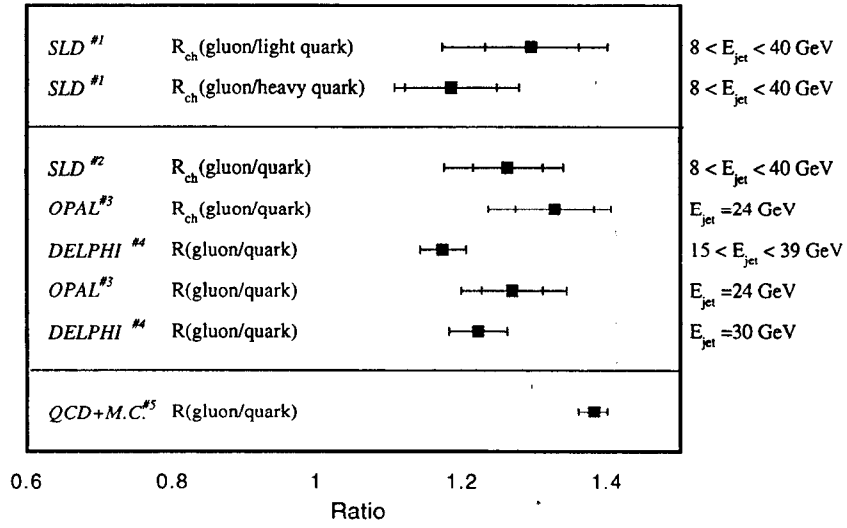

Figure 6.1: Summary of recent measurements of the multiplicity ratio. #1:The results of this analysis. #2:Obtained by combining our results of $R_{ch}(gluon/light\,quark)$ and $R_{ch}(gluon/heavy\,quark)$ with the ratio of $\text{Br}(Z^0 \to light\,quarks)$ and $\text{Br}(Z^0 \to heavy\,quarks)$. #3:[5]. #4:No systematic error is quoted[6]. #5:[1].

QCD prediction.

$\langle X_E \rangle$ of gluon jets is found to be smaller than those of light and heavy quark jets. Thus gluon jets have softer energy spectrum than quark jets as expected in QCD naively. $\langle \theta \rangle$ of gluon jets is also wider than those of light and heavy quark jets. This is consistent with qualitative QCD expectation.

In conclusion, we observed differences in global jet properties between quark and gluon jets using Z^0 hadronic 3-jet events. These results are in agreement with QCD expectations.

Bibliography

[1] I. M. Dremin and R. C. Hwa, Average multiplicities in gluon and quark jets as exact solution of QCD equations, Phys. Lett. B 324(1994)477-481

[2] JADE Collaboration, W. Bartel et. al., Experimental evidence for differences in $\langle p_\perp \rangle$ between quark jets and gluon jets, Phys. Lett. 123B(1983)460;
UA2 Collaboration, P. Bagnaia et. al., Measurement of jet fragmentation properties at the CERN $\bar{p}p$ collider, Phys. Lett. 144B(1984)291;
Mark II Collaboration, A. Peterson et. al., Inclusive charged-particle distribution in nearly threefold-symmetric three-jet events at $E_{c.m.} = 29$ GeV, Phys. Rev. Lett. 55(1985)1954;
UA1 Collaboration, G. Arnison et. al., Analysis of the fragmentation properties of quark and gluon jets at the CERN SPS $p\bar{p}$ collider, Nucl. Phys. B276(1986)253;
TASSO Collaboration, W. Braunschweig et al., Z. Phys. C45(1989)1;
AMY Collaboration, Y. K. Kim et al., Comparison of quark and gluon jets produced in high-energy e^+e^- annihilations, Phys. Rev. Lett. 63(1989)1772;

[3] HRS Collaboration, M. Derrick et. al., Phys. Lett. B 165(1985)449.

[4] OPAL Collaboration, G. Alexander et. al., A direct observation of quark-gluon jet differences at LEP, Phys. Lett. B265(1991)462;

[5] OPAL Collaboration, P. D. Acton et. al., A study of differences between quark and gluon jets using vertex tagging of quark jets, CERN-PPE/93-02, Z. Phys. C58(1993)387.

[6] Stefan Überschär(DELPHI collaboration), talk presented at the 8th DPF Meeting, Albuquerque, New Mexico, 1994.

[7] E. D. Commins and P. H. Bucksbaum, Weak interactios of leptons and quarks; G. Kane, Modern elementary particle physics,;

[8] Particle Data Group, L. Montanet et al., Phys. Rev. D 50(1994).

[9] Richard D. Field, Applications of perturbative QCD, Redwood City, USA: Addison-Wesley(1989).

[10] Donald H. Perkins, Introduction to high energy physics, Third Edition.

[11] G. Preparata, Why are quarks(and gluons) confined?, MITH93/18.

[12] CDF Collaboration, F. Abe et. al., Evidence for top quark production in $p\bar{p}$ collisions at $\sqrt{s} = 1.8$ TeV, FERMILAB-PUB-94/097-E, Phys. Rev. D50(1994)2966.

[13] J. B. Gaffney and A. H. Mueller, Nucl. Phys. B 250(1985)109.

[14] G. Marchesini et al., Comp. Phys. Comm. 67(1992)465.

[15] Yoshihito Iwasaki(SLD collaboration), talk presented at the 8th DPF Meeting, Albuquerque, New Mexico, 1994, SLAC-PUB-6597, TOHOKU-HEP-94-02.

[16] Thomas D. Gottschalk, Hadronizatin and fragmentation, CALT-68-1075.

[17] P. Mättig, The structure of jets in e^+e^- collisions, Physics Reports(Review section of Physics Letters) 177, Nos 3&4(1989)141-317.

[18] G. Altarelli and G. Parisi, Nucl. Phys. B 126(1977)298.

[19] J. Ellis, M. K. Gaillard and G. G. Ross, Nucl. Phys. B111(1976)253.

[20] A. Ali, J.G. Körner, Z. Kunszt, E. Pietarinen, G. Kramer, G. Schierholz and J. Willrodt, Nucl. Phys. B167(1980); R. K. Ellis, D. A. Ross and E. A. Terrano, Nucl.

Phys. B178(1981)421; K. Fabricius, G. Kramer, G. Schierholz and I. Schmitt, Z. Phys. C11(1982)315; F. Gutbrod, G. Kramer and G. Schierholz, Z. Phys. C21(1984)235.

[21] Torbjörn Sjöstrand, The LUND Mote Carlo for jet fragmentation and e^+e^- physics - JETSET version 6.2, Comput. Phys. Commun. 39(1986)347-407.

[22] R. D. Field and S. Wolfram, Nucl. Phys. B 213(1983)65.

[23] L. Lönnblad, Comput. Phys. Commun. 71(1992) 15; U. Pettersson,'ARIADNE, A Monte Carlo for QCD cascades in the colour dipole formulation', LU TP 88-5(1988).

[24] G. Gustafson, Phys. Lett. B 175(1986) 453

[25] T. Sjöstrand, QCD generators, Z Physics at LEP 1, CERN 89-08, Volume 3 (1989)

[26] G. Blaylock. The WISRD beam energy measurement. SLD Physics Note 22, SLAC(June 1993); J. Kent et al. SLAC-PUB-4922(March 1989).

[27] SLD Collaboration. First measurement of the left-right cross section asymmetry in Z boson production by e^+e^- collisions. Phys.Rev.Lett, 70(17):2515(1993)

[28] SLD Collaboration. Precise measurement of the left-right cross-section asymmetry in Z boson production by e^+e^- collisions. Phys.Rev.Lett, 73(17):25-29(1994)

[29] SLD Design Report, SLAC-Report-273(1984)

[30] M.G. Strauss et al., in the proceedings fo the 7th Meeting of the American Physical Society, Division of Particles and Fields, p. 1758. G. Charpak and F. Sauli, Annu. Rev. Nucl. Part. Sci. 34:285(1984).

[31] Jan A. Lauber, A study of jet rates and measurement of α_s at the Z^0 resonance. Ph.D thesis.

[32] GEANT 3.15 program, CERN Application Software Group, CERN Program Library(1993).

[33] TASSO Collaboration, W. Braunschweig et. atl., Z. Phys. C41 359(1988); P. N. Burrows, Z. Phys. C41, 375(1988).

[34] OPAL Collaboration, M. Z. Akrawy et al., Z. Phys. C47, 505(1990).

[35] C. Peterson, D. Schlatter, I. Schmitt and P. M. Zerwas, Phys. Rev. D27 105(1983).

[36] ALEPH Collaboration, D. Buskulic et. al., Z. Phys. C62 179(1994); L3 Collaboration, B. Adeva et. al., Phys. Lett. B261 177(1992); OPAL Collaboration, R. Akers et. al., Z. Phys. C61 209(1994); DELPHI Collaboration, P. Abreu et. al., Z. Phys. C59 533(1993).

[37] OPAL Collaboration, P. D. Acton et. al., Z. Phys. C53 539(1992).

[38] SLD Collaboration, K. Abe et. al, Measurement of R_b with impact parameters and displaced vertices, SLAC-PUB 6569.

[39] N. Isgur, D. Scora, B. Grinstein and M. B. Wise, Phys. Rev. D39 799(1989).

[40] M. Artuso(CLEO Collaboration), HEPSY-7-93, talk presented at Workshop on b Physics at Hadron Accelerators(1993).

[41] CLEO Collaboration, G. Crawford et. al., Phys. Rev. D45 725(1992).

[42] F. Muheim(CLEO Collaboration), talk presented at the 8th DPF Meeting, Albuquerque, New Mexico, 1994.

[43] ARGUS Collaboration, H. Albrecht et. at., Z. Phys. C58 191(1993); ARGUS Collaboration, H. Albrecht et. at., Z. Phys. C62 371(1994).

[44] David C. Williams, The left-right forward-backward asymmetry for b quarks at the SLD. Ph.D thesis.

[45] John M. Yamartino, Hadronic event selection using the LAC, SLD Physics Note No. 14.

[46] H.Park, R. Ben David, R. Dubois, R. Frey and P.C. Rowson, Event selection for the 1992 A_{LR} analysis, SLD Physics Note No. 17.

[47] Vernon D. Barger and Roger J. N. Phillips, Collider Physics, Redwood City, USA: Addison-Wesley(1987).

[48] Jan A. Lauber, Ph.D Thesis, SLAC-Report-413(1993).

[49] R. Ben-David, H. Park, Background Measurement for the 1992 A_{LR} Analysis, SLD Physics Note No. 18.

[50] S. Cantani et al., Phys. Lett. B 269(1991) 432; N. Brown and W. J. Stirling, Z. Phys. C 53(1992) 629; S. Bethke, Z. Kunszt, D. Soper and W. J. Stirling, Nucl. Phys. B 370(1992) 320.

[51] SLD Collaboration, K. Abe et al., A Measurement of $R_b = \frac{\Gamma(Z^0 \to b\bar{b})}{\Gamma(Z^0 \to hadrons)}$ at SLD, SLAC-PUB-6292(1993).

[52] SLD Collaboration, K. Abe et al., Measurement of the charged multiplicity of $Z^0 \to b\bar{b}$ events, Phys. Rev. Lett., 72(20):3145-3149(1994).

Appendix A

SLD Collaboration

- Adelphi University

  Robert Steiner

- INFN Sezione di Bologna

- Brunel University

  Adrian McKemey, Steve Watts, Nicholas Allen, Erez Etzion

- Boston University

  John Coller, James Shank, J. Scott Whitaker, Sarah Hedges

- University of Cincinnati

  Brian Meadows, Mirko Nussbaum

- California Institute of Technology

- University of Colorado

  Gregory Baranko, Nety Krishna, Uriel Nauenberg, Kathy Oliver, Cheng-Gang Fan

- Columbia University

  Michael Shaevitz, Srinka Ghosh, John Son, Peter Rowson

- Colorado State University

  Bob Wilson, Mihai Dima

- INFN Sezione di Ferrara

  Barbara Camanzi, Edoardo Mazzucato, Livio Piemontese

- Lab. Nazionali di Frascati

  Alessandro Calcaterra, Riccardo Desangro, Ida Peruzzi, Marcello Piccolo

- University of Illinois

  Bob Eisenstein, Gary Gladding, Inga Karliner, Andrew Foland

- KEK National Lab

- Lawrence Berkeley Laboratory

  Bruce Schumm, Gil Shapiro, Herbert Steiner

- Louisiana Technical University

  Kathleen Johnston, Basem Barakat, Jeff Smith, Eric Burch

- University of Massachusetts

  Stanley Hertzbach, Richard Kofler, Michael Strauss, Aurel Trandafir

- University of Mississippi

  Robert Kroeger, Jim Reidy

- Massachusetts Institute of Technology

  Philip Burrows, Sandra Fowler, Henry Kendall, Louis Osborne, Dale Ross, Frank Taylor, Robin Verdier, Ray Cowan, Michael Fero, Jim Quigley, Eric Torrence, Richard Yamamoto, Zhibo Zhang

- Nagoya University

  Ryoichi Kajikawa, Akira Sugiyama, Shiro Suzuki, Yukiyoshi Ohnishi, Kenji Abe

- Northeastern University

- University of Oregon

  Jim Brau, Raymond Frey, Jingchen Zhou, Jennifer Huber, Matthew Langston, Xiaoxing Yang, Nikolai Sinev, Hyun Hwang

- Universita di Padova

- Universita di Perugia, Sezione INFN

  Giampiero Mancinelli, Giancarlo Mantovani, Donatella Falciai, Roberto Massetti

- INFN, Sezione di Pisa

- Rutherford Appleton Laboratory

  Chris Damerell, Tony Gillman, Fred Wickens, David Jackson

- Rutgers University

  Kenneth Baird, Pieter Jacques, Mohan Kalelkar, Richard Plano, Peter Stamer

- Stanford Linear Accelerator Center

  Daniel Alzofon, Jack Hoeflich, Bill Wisniewski, Xiaofan Zhou, David Calloway, Emlyn Hughes, Ross King, Thomas Markiewicz, Takashi Maruyama, Hiroaki Masuda, Kenneth Moffeit, Charles Prescott, Leon Rochester, Owen Saxton, Morris Swartz, Tracy Usher, Charles Young, Mike Woods, Mourad Daoudi, Andrea Davies, David Aston, Hideaki Kawahara, David Leith, Matt McCulloch, Don McShurley, David Muller, Gerard Oxoby, Tom Pavel, Blair Ratcliff, Robert Reif, Constantine Simopoulos, Paul Stiles, Jaroslav Vavra, Tom Weber, Malcolm Lewis, Lilian DePorcel, Paul Rensing, Thomas Mattison, Alexei Tolstykh, Colin Jessop, Stephen Schaffner, Mary King, John

Jaros, Dong Su, Tom Junk, Rafe Schindler, Homer Neal, Bill Burgess, Wesley Craddock, Vickee Flynn, David Burke, Michael Hildreth, Greg Punkar, Steve Wagner, Timothy Barklow, Richard Boyce, Stephen Williams, Barbara Barrera, Joanne Bogart, Gary Bower, Martin Breidenbach, Ronald Cassell, Bernie Culver, Richard Dubois, Justin Escalera, Dietrich Freytag, Mark Freytag, Gunther Haller, Vern Hamilton, Karen Heidenreich, John Hodgson, Mike Huffer, Harvey Lynch, Robert Messner, Len Moss, Kazuko Onaga, Joseph Perl, Gerard Putallaz, James Russell, Philip Seward, Stephen Smith, Anthony Waite, Ramon Berger, Kris Dudley, Michael Foss, Jessie Gutierrez, Gibson Locke, Raymond Rodriguez, Donald Peterson, Takashi Akagi, Skappass VIII Knut, Anthony Johnson, Eric Vella, Aaron Chou, Glen Crawford, Howard Rogers, James Davis, Gregory Rogers

- Sogang University

  Yongduk Kim, Hyejoo Kang, Dongwk Hwang

- University of Tennessee

  Steve Berridge, Bill Bugg, Hans Cohn, Peter Du, Hilman Hargis, Edward Hart, Achim Weidemann, Sharon White, Konstantine Shmakov

- Tohoku University

  Koya Abe, Yoji Hasegawa, Kazumi Hasuko, Yoshihito Iwasaki, Tadashi Nagamine, Shinya Narita, Fumihiko Suekane, Haruo Yuta

- U.C. Santa Barbara

  Debbie Ceder, Adolph Lu, Steven Yellin

- U.C. Santa Cruz

  Guy Blaylock, Don Coyne, Georgia Hamel, Xi Liu, Terry Schalk, Michael Schneider, David A. Williams, James Mattingly

- Vanderbilt University

  Robert Panvini, Terry Reeves, John Venuti

- University of Washington

  Toby Burnett, Victor Cook, Ji Ma, Paul Mockett, Anthony Szumilo, Eric Church, Eric Weiss

- University of Wisconsin

  Henry Band, Jim Johnson, Richard Prepost, Geordie Zapalac, Victor Serbo

- Yale University

  Charles Baltay, William Emmet, Steven Manly, Jeffrey Snyder, Stephane Willocq, Sumit Sen, Jinchun Kou, Ming Liu

Appendix B

Systematic Errors

In this appendix, we examine the experimental systematic errors of the ratios obtained in previous section. The systematic errors are the experimental biases introduced by the detector acceptance, efficiency and resolution, and by the detector simulation, event reconstruction, and by the several selection criteria applied to the data for this analysis, and by the bottom and charm quarks parameters used in M.C. simulation which are used for the jet flavour tagging, unfolding and corrections. The possible systematic error sources are divided into five categories as follows.

1. Track and event selection

   For the track and event selection category, we apply the tight cuts of the selection criteria one by one to see the sensitivity on the cut values. Loose cuts are not applied because the disagreements between the data and the M.C. are observed in the region of the loose cuts, and may cause imperfect corrections of the detector acceptance and efficiency. In Table B.1, the variations of the selection criteria are listed. Each set of variations are applied for both the data and the M.C with the same analysis procedure, and then compared against the standard cuts

$$\Delta R = R_{var} - R_{std}, \tag{B.1}$$

Systematic Errors

Categories / Sources	Cuts: Standard	Cuts: Variations	$\langle n_{ch} \rangle$ $\Delta R^{C/L}_{syst.}$ / $\Delta R^{C/H}_{syst.}$	$\langle X_E \rangle$ $\Delta R^{C/L}_{syst.}$ / $\Delta R^{C/H}_{syst.}$	$\langle \theta \rangle$ $\Delta R^{C/L}_{syst.}$ / $\Delta R^{C/H}_{syst.}$
Track and event selection					
$\lvert\cos\theta\rvert$	0.7	0.8	~ 0 / ~ 0	~ 0 / ~ 0	~ 0 / ~ 0
P_t (GeV)	0.15	0.30	-0.047 / -0.035	$+0.070$ / $+0.042$	-0.023 / ~ 0
$\lvert\cos\theta_{thrust}\rvert$	0.70	0.40	~ 0 / ~ 0	$+0.015$ / -0.042	-0.008 / ~ 0
E_{vis} (GeV)	18.2	30.0	~ 0 / ~ 0	~ 0 / ~ 0	~ 0 / ~ 0
# of good tracks	5	7	~ 0 / ~ 0	~ 0 / ~ 0	~ 0 / ~ 0
sub-total			± 0.047 / ± 0.035	± 0.072 / ± 0.060	± 0.024 / ~ 0
Detector modeling					
varying p		$\Delta p/p = 0.6\%$	~ 0 / $+0.027$	~ 0 / ~ 0	~ 0 / ~ 0
removing tracks		3.5%	~ 0 / ~ 0	~ 0 / ~ 0	$+0.032$ / ~ 0
sub-total			~ 0 / $+0.027$	~ 0 / ~ 0	$+0.032$ / ~ 0
3-jet event selection					
y_{cut}	0.007	± 0.001	~ 0 / ~ 0	~ 0 / ~ 0	~ 0 / ~ 0
$\sum \varphi_i$ (degree)	358	± 1	~ 0 / ~ 0	~ 0 / ~ 0	~ 0 / ~ 0
$\lvert\cos\theta_{jet}\rvert$	0.7	± 0.05	~ 0 / $+0.051$ / ~ 0	-0.029 / -0.049 / ~ 0	~ 0 / -0.032 / ~ 0
E^{vis} (GeV)	5.0	± 1.0	~ 0 / ~ 0	~ 0 / ~ 0	~ 0 / ~ 0
sub-total			~ 0 / $+0.051$	-0.029 / -0.049	~ 0 / -0.032
Jet tagging					
$\sigma^{imp}_{sig.}$	3	± 1	~ 0 / ~ 0	$+0.010$ / ~ 0	~ 0 / ~ 0 / -0.031
# of significant tracks	2	± 1	-0.018 / -0.039 / ~ 0	~ 0 / -0.011 / ~ 0	~ 0 / ~ 0 / -0.034
sub-total			-0.043 / ~ 0	$+0.015$ / $+0.009$	~ 0 / $+0.009$ / -0.046
Monte Carlo model					
B meson lifetime (ps)	1.55	± 0.1	~ 0 / ~ 0	~ 0 / ~ 0	~ 0 / ~ 0
b baryon lifetime (ps)	0.80	± 0.3	~ 0 / ~ 0	~ 0 / ~ 0	~ 0 / ~ 0
varying $\mathrm{Br}(B \to D + X)$		$\pm 1\sigma$	~ 0 / ~ 0	~ 0 / ~ 0	~ 0 / ~ 0
c fragmentation (X_E)	0.494	± 0.025	~ 0 / ~ 0	~ 0 / ~ 0	~ 0 / ~ 0
sub-total			~ 0 / ~ 0	~ 0 / ~ 0	~ 0 / ~ 0
Total			$+0.047$ / -0.064 / $+0.068$ / -0.035	$+0.073$ / -0.077 / $+0.061$ / -0.077	$+0.040$ / -0.024 / -0.056

Table B.1: Systematic errors. The total is a quadratic sum of each source.

Appendix C

Monte Carlo Models

In this appendix, we compare our results with M.C. models, described in 2.4. The M.C. models, we use in this analysis, are the Jetset 6.3, the Herwig 5.7 and the Ariadne 4.06, which are commonly used in many e^+e^- experiments. These generators create the hard partons(quarks and gluons) in Z^0 decay, and then partons make parton showers to low energy, followed by string, cluster and color dipole hadronization models for the Jetset, the Herwig and the Ariadne, respectively. In the Ariadne, the electro-weak interaction phase of e^+e^- and the hadronization model are not implemented. Therefore the Jetset is used to simulate those phases.

The main parameters of these M.C. models are listed in Table 3.6, C.1, C.2 for the Jetset, the Herwig, and the Ariadne, respectively. In Table C.1 and C.2, the parameter Λ_{QCD} control the branching in the parton shower. m_g is the effective gluon mass and M_{max}

Parameter	Name	Default	Optimized value
Λ_{QCD}	QCDLAM	0.18 GeV	0.11 GeV
m_g	RMASS(13)	0.75 GeV	0.65 GeV
M_{max}	CLMAX	3.35 GeV	3.00 GeV

Table C.1: Main parameters of the HERWIG 5.7.

Monte Carlo Models

Parameter	Name	Default	Optimized value
Λ_{QCD}	PARA(1)	0.22 GeV	0.22 GeV
$p_\perp$	PARA(3)	0.60 GeV	0.60 GeV

Table C.2: Main parameters of the ARIADNE 4.06.

is the maximum mass of a cluster. $p_\perp$ is the cut-off in invariant $p_\perp$ for gluon emissions from color dipoles. In this analysis, the default parameters are used for the Ariadne.

The M.C. data are generated without any detector simulation. Jets are determined by the Durham jet finder with $y_{cut} = 0.007$, and jets are tagged by the generator information. The M.C. distributions of $\langle n_{ch} \rangle$, $\langle X_E \rangle$, $\langle \theta \rangle$ at the hadron level are shown in Fig. C.1, C.2 and C.3 respectively, where plots (a), (b) and (c) are gluon jets, light quark jets and heavy quark jets, respectively. Plots (d) and (e) are the ratios of gluon jets to light quark jets and gluon jets to heavy quark jets, respectively. In these plots, our experimental results are also shown.

In the $\langle n_{ch} \rangle$ comparison(Fig. C.1), the Jetset describes the data well in all plots((a), (b) and (c)), except for the last bin. The Ariadne reproduces the gluon jets $\langle n_{ch} \rangle$, however, the multiplicities of light quark jets are overestimated in all energy region. $\langle n_{ch} \rangle$ of heavy quark jets of the Ariadne is similar to the Jetset because the Ariadne uses the package of heavy hadron decay in the Jetset[1] and $\langle n_{ch} \rangle$ of heavy quark jet is dominated by the decay of heavy hadrons. The multiplicities of the Herwig is systematically higher than those of data. In the ratio plots(Fig. C.1 (d) and (e)), the Jetset and the Herwig have good agreements with the data, while the ratio of the Ariadne are almost unity in all energy regions, these are differ from the data. In Table C.3, the reduced χ^2 for each generator are listed.

In the $\langle X_E \rangle$ comparison(Fig. C.2), we can see anti-correlation between $\langle n_{ch} \rangle$ and $\langle X_E \rangle$. The Ariadne and the Herwig have softer energy fractions in light quark and heavy

[1]See chapter 3.3

Monte Carlo Models

quark jets, respectively, in comparison with the data. The Jetset well reproduces the energy fraction distribution. In the ratio plots(Fig. C.2 (d) and (e)), the Jetset and the Herwig agree with the data. The ratios of both gluon to light and heavy quarks of the Ariadne are almost unity, as $\langle n_{ch} \rangle$, thus ARIADNE does not agree with the data.

In Fig. C.3, $\langle \theta \rangle$ of the data and M.C. are compared. All of three M.C. models describe $\langle \theta \rangle$ of gluon jets well. $\langle \theta \rangle$ of light quark and heavy quark are also well reproduced. However, the Ariadne is relatively wider and HERWIG is narrower than the data.

In conclusion, our data are well reproduced by the Jetset, in comparison of average charged multiplicity, inclusive energy distribution, and jet width. The Herwig describes light quark and gluon jets well, however, disagreement are found in the properties of heavy quark jet. In the Ariadne, there is no differences between quark jets and gluon jets. Therefore, the Ariadne is not consistent with our data.

Monte Carlo Models

Observable	Jet flavour	Jetset 6.3	Herwig 5.7	Ariadne 4.06
$\langle n_{ch} \rangle$				
	Gluon Jets	1.8	3.5	2.5
	Light Quark Jets	5.4	6.0	14.2
	Heavy Quark Jets	1.4	7.1	1.2
	Ratio(Gluon/Light Quark)	2.8	2.7	6.8
	Ratio(Gluon/Heavy Quark)	1.7	2.8	3.0
$\langle X_E \rangle$				
	Gluon Jets	2.4	3.9	7.4
	Light Quark Jets	6.3	7.0	16.4
	Heavy Quark Jets	1.4	5.7	1.1
	Ratio(Gluon/Light Quark)	5.6	5.7	25.6
	Ratio(Gluon/Heavy Quark)	3.6	6.6	10.4
$\langle \theta \rangle$				
	Gluon Jets	2.1	2.2	2.3
	Light Quark Jets	2.4	2.0	4.0
	Heavy Quark Jets	0.7	1.8	3.1
	Ratio(Gluon/Light Quark)	1.7	1.6	2.1
	Ratio(Gluon/Heavy Quark)	0.3	1.1	1.9

Table C.3: χ^2/N_{df} of M.C. model comparison.

Monte Carlo Models

Monte Carlo Models

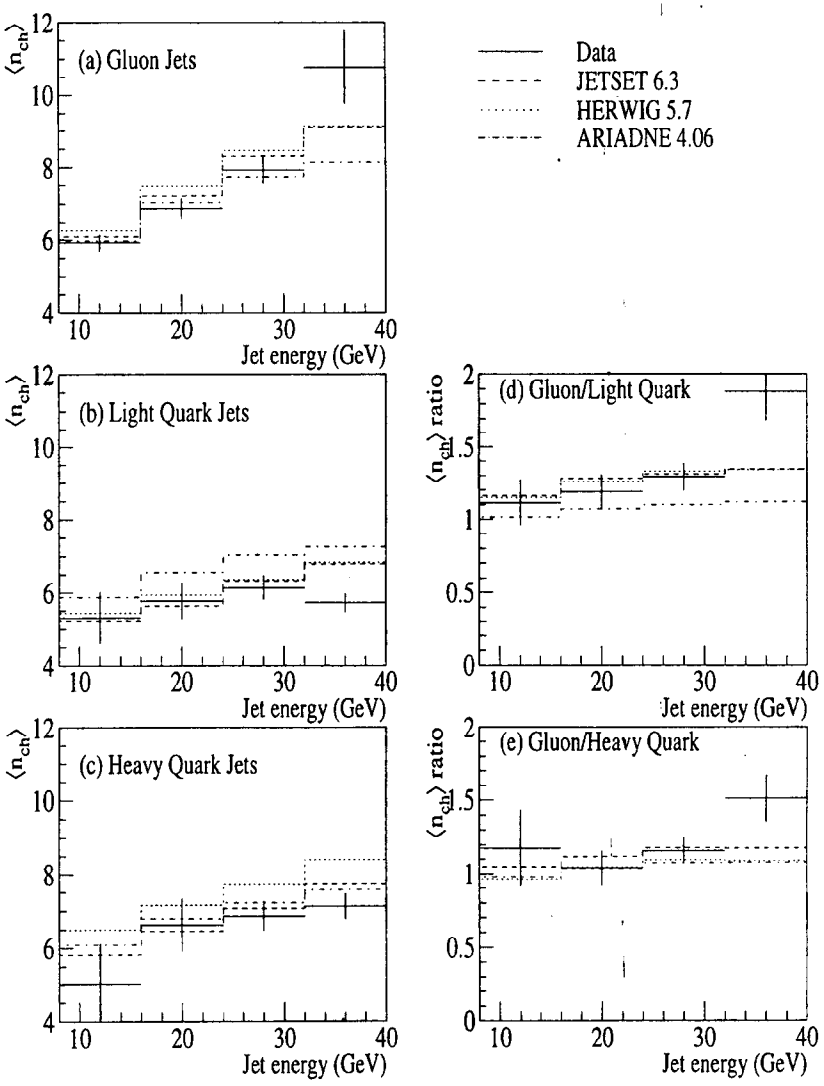

Figure C.1: M.C. comparison of $\langle n_{ch} \rangle$.

Monte Carlo Models

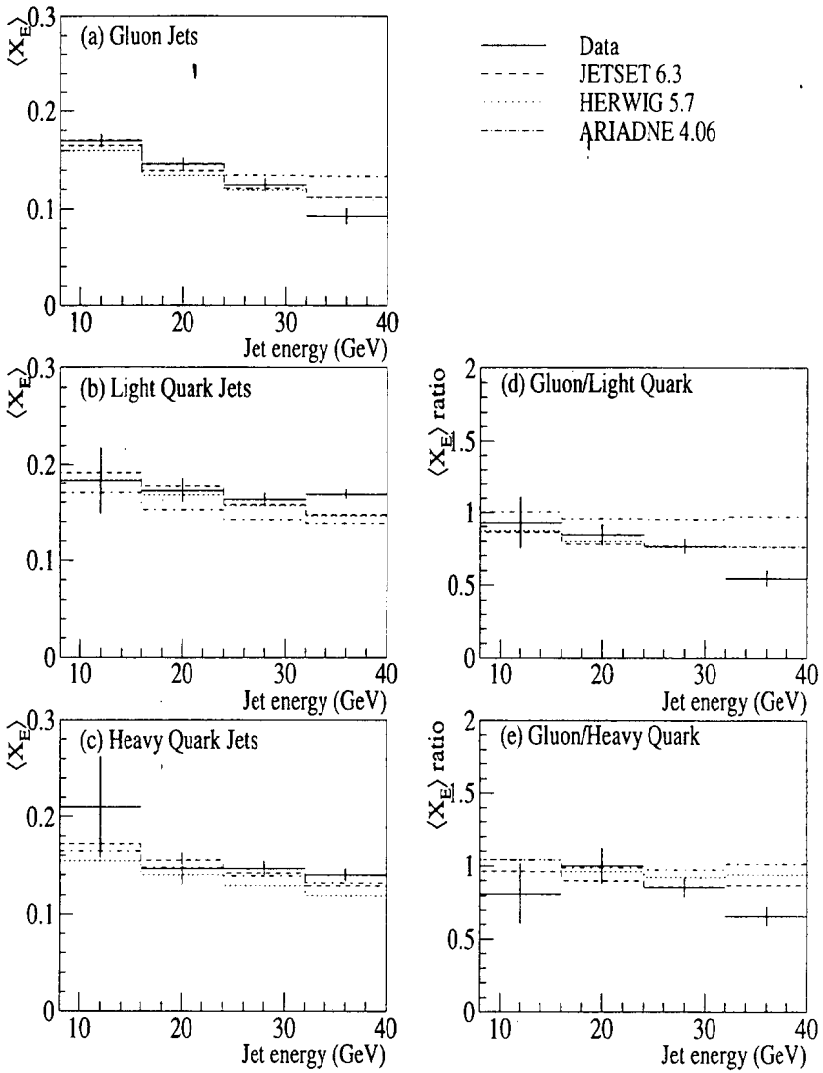

Figure C.2: M.C. comparison of $\langle X_E \rangle$.

Monte Carlo Models

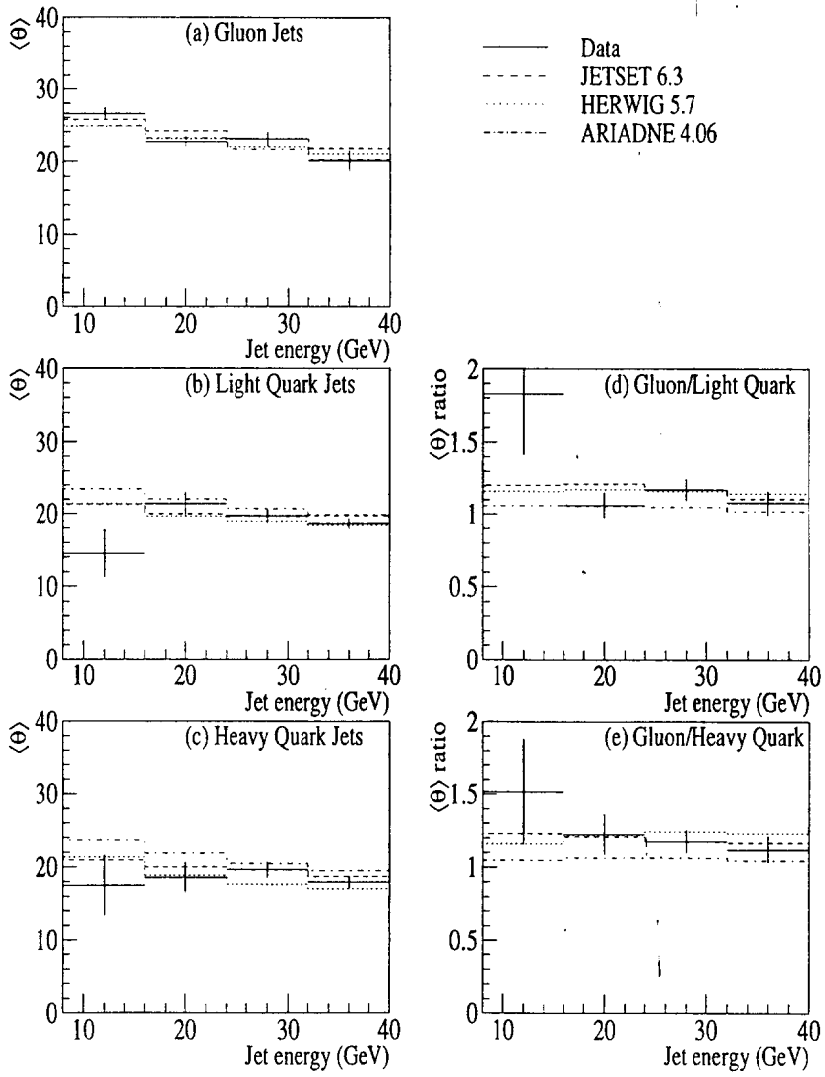

Figure C.3: M.C. comparison of $\langle \theta \rangle$.

Appendix D

Quark jet purity of the highest energy jet

In chapter 5.2, we assume that the highest energy jet in a 3-jet event is a quark jet. This is due the bremsstrahlung nature of gluon radiation. This natural assumption is used in the selection of three jet samples: the gluon tagged, the light mixture, and the heavy mixture. In this appendix, we consider the quark jet purity of the highest energy jet in 3-jet events.

Fig. D.1 shows the energy spectra of jet 1, jet 2, and jet 3 in 3-jet events. The jets are ordered by a kinetic jet energy(see chapter 5.1). In the jet energy range from 30 GeV to 45 GeV, the energy spectra of jet 1 and jet 2 overlap. Thus, there is an ambiguity in the determination of the highest energy jet in the energy range due to a small jet energy difference and finite jet energy resolution. However, events including such jet 1 and jet 2 are symmetric or nearly symmetric, and have a third jet with small jet energy. Such a jet with small jet energy may be a gluon jet, and thus two higher energy jets can be quark jets. Therefore, we consider that the jet energy overlap of jet 1 and jet 2 are not significant for the assumption. In Fig. D.1, gluon components obtained by the Monte Carlo are also plotted. The purity of quark jet in the highest energy jet is 93.5%, and the gluon contamination is 6.5%.

In order to estimate quark jet purity of the highest energy jet in data, we use the jet

flavour tagging. In Table D.1, fractions of heavy tagged jets in jet 1, 2, and 3 are listed. The fractions of the data and Monte Carlo are in good agreement. In jet 1, the fraction of heavy tagged jets is $(14.5 \pm 0.5)\%$ and is equal to sum of the fractions of jet 2 and 3 within a statistical error. If we assume that the tagging purity and efficiency is independent of the jet number, this indicates that the number of heavy quark jets in jet 1 is equal to that in jet 2 and 3.

Using the M.C. simulation, purities and efficiencies of heavy flavour tagging are estimated. The fraction of heavy flavour quark(c and b) jets in each jet, R_{heavy}, is calculated by

$$R_{heavy} = \frac{R_{tagged} \cdot p}{\epsilon}, \tag{D.1}$$

where R_{tagged} is the fraction of the heavy tagged jets, p and ϵ are the purity and efficiency, respectively. If we assume that the ratio of heavy flavour quark to all flavour are the same as the ratio in Z^0 decay, it is possible to calculate the fraction of all flavour quark(d, u, s, c, and b) jets in each jet:

$$R_{quark} = R_{heavy}/B, \tag{D.2}$$

where R_{quark} is the fraction of all flavour quark jets, and

$$\begin{aligned} B &= \frac{B_r(Z^0 \to c\bar{c}, b\bar{b})}{B_r(Z^0 \to d\bar{d}, u\bar{u}, s\bar{s}, c\bar{c}, b\bar{b})} \\ &= \frac{0.119 + 0.155}{0.699} \\ &= 0.392, \end{aligned} \tag{D.3}$$

where the values of Z^0 branching ratios are listed in Table 2.1.

The estimated fraction of quark jets in jet 1, listed in Table D.2, is $93.6 \pm 4.3\%$. This value is good agreement with the value 93.5% obtained by the Monte Carlo simulation.

Jet number	Data	Monte Carlo		
	Fraction(%)	Fraction(%)	Purity(%)	Efficiency(%)
jet 1	14.5 ± 0.5	14.5 ± 0.2	91.1 ± 2.1	36.0 ± 0.7
jet 2	9.8 ± 0.4	9.3 ± 0.2	84.8 ± 2.4	28.8 ± 0.7
jet 3	4.1 ± 0.3	3.3 ± 0.1	90.4 ± 4.3	26.3 ± 1.0

Table D.1: Fraction of heavy tagged jets.

Jet number	Quark jet fraction	
	Heavy flavour(%)	All flavour(%)
jet 1	36.7 ± 1.7	93.6 ± 4.3
jet 2	28.9 ± 1.5	73.6 ± 4.1
jet 3	14.1 ± 1.3	36.0 ± 3.4

Table D.2: Fraction of quark jets.

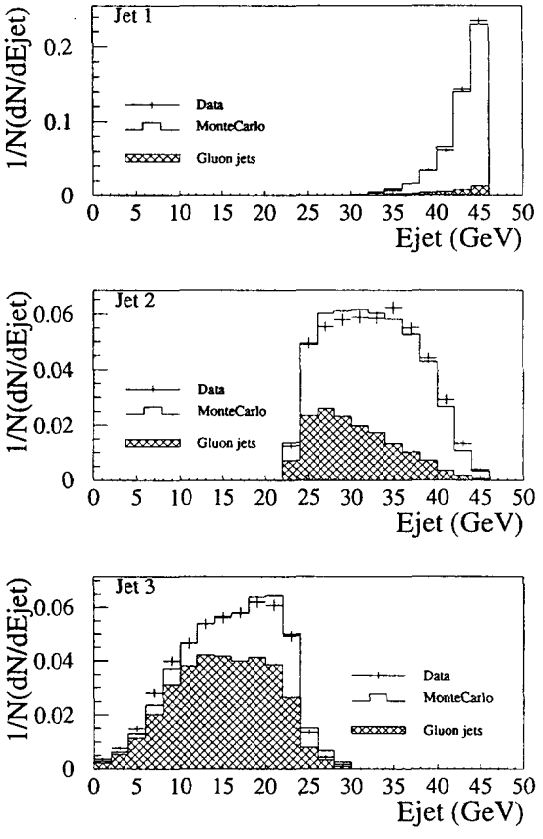

Figure D.1: Energy spectra of jets in 3-jet events